https://dx.doi.org/10.1016/j.ijplas.2023.103733

Unraveling size-affected plastic heterogeneity and asymmetry during micro-scaled deformation of CP-Ti by non-local crystal plasticity modelling

Xuefeng Tang[a], Zhizhou Wang[a], Lei Deng[a], Mao Zhang[a], Pan Gong[a], Junsong Jin[a], Xinyun Wang[a, *], M. W. Fu[b, *]

a State Key Laboratory of Materials Processing & Die and Mold Technology, School of Materials Science and Engineering, Huazhong University of Science and Technology, Wuhan, 430074, China

b Department of Mechanical Engineering, Research Institute for Advanced Manufacturing, The Hong Kong Polytechnic University, Hung Hom, Kowloon, Hong Kong, China

* Corresponding author: wangxy_hust@hust.edu.cn (Xinyun Wang), mmmwfu@polyu.edu.hk (M. W. Fu)

Abstract

Titanium alloy is prominent to manufacture high performance miniature device, whilst size-affected plastic heterogeneity and asymmetry in micro-scaled deformation are not well understood due to its complex deformation mechanism. How does the interplay among dislocation slip, deformation twinning, and strain gradient affect the size-dependent plastic heterogeneity and T-C asymmetry is an intractable and non-eluded issue which needs to be unravelled. In this research, a mechanism-based non-local crystal plasticity model incorporating dislocation and twinning mediated deformation was proposed and implemented into a finite element framework. The proposed non-local model successfully represents the size-dependent asymmetrical mechanical responding and texture evolution. Without considering GND, the grain size effect was weakened and twin activity is slow down and the relative activities of pyramidal<c+a> and basal slip are decreased. The size-dependent fracture behavior, plastic heterogeneity and T-C asymmetry during micro-scaled deformation of commercial pure titanium (CP-Ti) were explored by coupling micro-tension/compression test and full-field simulation. Results showed that T-C asymmetry in flow stress was enhanced with the increasing grain size and the decreasing diameter of specimen. In the sample with $D \geq 0.6$mm, the ductility of CP-Ti is enhanced with grain size due to the more prevailing twins since the concentrating stress could be relieved by such abundant slip rather than cracking. Grain-scale strain is more homogeneous in compression when d is increased from 60 to 110μm since more activation of non-prismatic slip that accommodates strain along various direction. The strengthen contributed from GND follows the Hall-Petch law and the SSD density at surface grains is generally lower than inner grains, leading to the soft layer near free surface. The width of soft layer is about one grain. This work provides an in-depth understanding of size-affected plastic heterogeneity and asymmetry during micro-scaled deformation of CP-Ti which supports

the forming of high-quality micro component under complex deformation path.

Keywords: ???????

1. Introduction

The rapid development of miniaturized devices and products places high demands on micro-components which can be processed by micro-scaled deformation. For the metallic micro-part, material is degenerated from polycrystals to the so-called oligocrystals, in which severe heterogenous inter and intragranular deformation are nonnegligible in plastic deformation (Demir and Gutierrez-Urrutia, 2021; Lim et al., 2014; Vasilev and Knezevic, 2021). Roughening surface, scattering deformation behaviors, anisotropic and asymmetric deformation behavior, and apparent size effect stemming from the downscaling make the precision and performance of micro-part difficult to guarantee (Fu and Wang, 2021; Tang et al., 2020; Vollertsen et al., 2006; Xu et al., 2021a; Zhang et al., 2021). Having in-depth understanding on the plastic heterogeneity at grain level and profound insight into the asymmetrical deformation at different scales are critical for improving the forming limit, forming quality, and performance of micro-scaled product.

Titanium alloys are extensively used in aerospace, weaponry, and bio-medical arenas due to their outstanding mechanical properties such as high strength-to-density ratio, fatigue and corrosion resistance, and excellent biocompatibility (Banerjee and Williams, 2013; Kaur and Singh, 2019). Many micro-components such as micro-channel (Xu et al., 2021b), micro-tube (Hartl, 2019), and dental abutment (Arentoft et al., 2011; Meng et al., 2016) have also been fabricated with titanium alloys. As a typical hexagonal close-packed (HCP) metal of low symmetry, titanium alloys have four primary slip systems: prismatic <**a**> $\left\{1\bar{1}00\right\}<11\bar{2}0>$, basal <**a**> $\{0001\}<11\bar{2}0>$, pyramidal <**a**> $\left\{1\bar{1}01\right\}<11\bar{2}0>$, and pyramidal <**c**+**a**> $\left\{10\bar{1}1\right\}<11\bar{2}3>$ (Britton et al., 2015; Hama et al., 2017; NEMAT-NASSER et al., 1999; Zaefferer, 2003). But the critical resolved shear stress (CRSS) of each family of slip systems differ significantly and slip with <**c**+**a**> Burgers vector is hard to operate at low temperature. Dislocation slip with <**a**> Burgers vector alone cannot provide five independent slip systems necessary to fulfill the von Mises criterion and maintain intergranular strain compatibility (Cepeda-Jiménez et al., 2015; Christian and Mahajan, 1995; Taylor, 1938; Yoo, 1981). Deformation twinning is then prevalently activated to accommodate plastic strain along the c-axis of crystal by creating heterogeneous lamellar shaped domains where both the lattice reorientation and shear localization are abrupt (Clausen et al., 2008; Kumar and Beyerlein, 2020; Kumar et al., 2018; Paramatmuni et al., 2020; Wroński et al., 2022). Such directional slip and polar deformation twinning lead to the strong anisotropic and asymmetric plasticity of titanium alloys which rends performance control difficult.

Tension-compression (T-C) asymmetry is one of the issues hampering the forming and application of HCP components (Suryawanshi et al., 2021; Yin et al., 2021). Numerous researches have been devoted to exploring the asymmetric response of HCP alloys. The T-C asymmetry behavior has a significant dependency on the microstructures, orientation, element concentration, and load conditions including temperature, strain rate, and strain path (Habib et al., 2017; Hama et al., 2015; Kurukuri et al., 2014; Syed et al., 2019; Tao et al., 2019; Yang et al., 2020; Yin et al., 2021). Significant T-C asymmetry in the RD was reduced by increasing the deformation temperature and decreasing the strain rate (Habib et al., 2017). Lin et al. (2017) reported that the stronger effect of grain refinement and texture hardening by lattice reorientation on compression than on tension leads to the T-C asymmetry in strain hardening. The X-ray tomography measurements performed by Revil-Baudard et al. (2016) reveal that the damage evolution of α-Ti specimens is drastically different from that of copper material, and there is a very strong correlation between the asymmetry of the plastic deformation and the rate of damage growth.

Most of the existing investigations on the plastic anisotropy and asymmetry were carried out for the large size part. While the deformation behavior may manifest differently at various scales and the knowledge gained at one scale cannot be directly transferred to another scale (Efstathiou et al., 2010; Fu et al., 2016). The downscaling of the part makes the geometric dimension comparable with the microstructural grains. As a result, grain scale plastic heterogeneity and various slip/twinning activities could significantly affect the overall anisotropic and asymmetric deformation and fracture behavior. Guo et al. (2020) found that the earing in deep drawing of TWIP steel at micro scale is obviously higher than that at macro scale. Meng et al. (2019) found that the plastic anisotropy of SUS304 foil was prominently enhanced with decreasing thickness and macroscale yield criterion failed to predict the anisotropic behavior when the grain size was of the same magnitude as foil thickness. For titanium alloys, the interaction among slip, twinning, and grain boundaries (GBs) make the size-dependent plastic heterogeneity and asymmetry in micro-components more complex. Our recent work found that the strain heterogeneity of pure titanium was more serious than that of copper and iron in micro-tension due to its multidirectional slip/twinning systems with different CRSS (Tang et al., 2019). In nano-scale, several researches have shown the nonnegligible size effect on the T-C asymmetry. Kim et al. (2012) reported that the T-C asymmetry in flow stress of single crystal Mo nano-pillar depends on crystallographic orientation and sample size, and the size-dependent T-C asymmetry is due to the relative shortage of screw dislocation. A significant

T-C asymmetry was also observed in Ni nanowire, where the T-C asymmetry in sample with larger wire radii decreases as the wire radius decreases and is reversed for the smallest wire (Monk and Farkas, 2007). To date, however, the experimental and modeling researches on the T-C asymmetric behavior of HCP polycrystalline in micro-scaled deformation are scarce. The synergistic effects of dislocation slip, deformation twining, and GBs on size-dependent plastic heterogeneity and T-C asymmetry during micro-scaled deformation of titanium alloys are still unclear.

Full-field crystal plasticity model is an advanced approach that is capable of correlating the deformation behavior with the underly microscopic mechanism from meso to macro scale (Flipon et al., 2020; Githens et al., 2020; Hestroffer et al., 2022; Marano et al., 2021; Ravaji and Joshi, 2021; Wijnen et al., 2021). It has been employed to explore the origins of strain localization and fracture of oligo-crystals (Baudoin et al., 2019; Yoshida, 2014; Zhao et al., 2008). In general, the GBs are not explicitly considered in crystal plasticity simulation and their impacts are reflected by crystallographic orientations. The strong grain neighbor effects (Abdolvand et al., 2018) in heterogeneous deformation of HCP metals would be underestimated. To quantitatively characterize the significant size effect, external length scale such as average grain size and sample diameter were usually introduced into the crystal plasticity model (Guo et al., 2020; Kim et al., 2018; Lu et al., 2020; Ravaji and Joshi, 2021; Tang et al., 2019; Venkatramani et al., 2007). In such a way, the dependency of macro mechanical response on grain size and geometrical size could be predicted. However, each grain has a different size and the morphology of crystals and external geometrical features change significantly under plastic deformation. Size-dependent meso scale strain and stress field, lattice rotation, and the slip/twinning activity would not be well described. This limitation can be overcome by introducing intrinsic length associated with strain gradient into the crystal plasticity model, i.e., the strain gradient or non-local crystal plasticity model (ARSENLIS and PARKS, 1999; Busso et al., 2000; Cheong et al., 2005; Counts et al., 2008; Dunne et al., 2007; Haouala et al., 2020; Ma et al., 2006). In the non-local model, the geometrically necessary dislocations (GND) are required to preserve crystallographic lattice compatibility that arises from inhomogeneous plastic deformation (Evers, 2004; Gurtin, 2002; Voyiadjis and Song, 2019). The hardening effects of short- and long-range obstacle could be modeled by the statistically stored dislocations (SSD) density and GND density based on their interactions and the gradient of plastic strain which depends on the deformation of neighboring regions (Cheng et al., 2018; Dunne et al., 2012; Sedaghat and Abdolvand, 2021). By using the non-local crystal plasticity model, Zhang and Dong (2015) found that both first order and second order size effect in microforming of copper could be described. Yalçinkaya et al

(2017) investigated the intrinsic and statistical size effect in microforming through a non-local crystal plasticity model and concluded that such method offers the physical modeling opportunity of inter-granular cracking since the stress concertation near the GBs for different grain size could be obtained.

Prior researches showed that the anisotropy and asymmetry behavior are more apparent with the downscaling of sample and could not be correctly predicted using macroscale yield criterion. Additional hardening and corresponding size effect caused by the interaction between dislocations and strain gradient could be predicted by the non-local crystal plasticity model. In regard of micro-scaled deformation of titanium alloy, however, the knowledge on size-dependent plastic heterogeneity and asymmetry is limited by lack of relevant studies. How do the microstructural grain and geometrical size affect the plastic heterogeneity and asymmetry, how about the T-C asymmetry in plastic heterogeneity at grain level, and what is the role of interplay among dislocation slip, deformation twining, and strain gradient on size-dependent plastic heterogeneity and T-C asymmetry is a puzzle that needs to be uncovered. In this research, a non-local crystal plasticity finite element (CPFE) model was established to describe the size-dependent asymmetrical mechanical response and texture evolution. Based on the micro-scaled tension/compression test and the full-field non-local CPFE simulation, the effect of intrinsic grain size and extrinsic geometrical size on the T-C asymmetry in the micro-scaled deformation of pure titanium were probed in terms of (1) global mechanical response and microstructure; (2) slip and twin activities; (3) size-dependent fracture behavior, (4) grain scale strain and stress pattern; and (5) dislocation density.

2. Experimental procedures

The as-received material in this work is a hot rolled and mill annealed polycrystalline commercial pure titanium (CP-Ti, grade 1). To investigate the effect of grain and geometrical size, the cylindrical compression sample and dog-bone tension sample with different diameters were prepared from the same bar by precision turning, as shown in Fig. 1. These samples were encapsulated in vacuum glass tube with a pressure of 3.0×10^{-4}Pa and then annealed at 600 °C, 700 °C, and 800 °C for 1h, respectively, to obtain different initial grain sizes. Fig. 2 shows the initial microstructure and pole figure of the sample treating at various temperatures. All of them are consisted of twin-free recrystallized grain structure and the average grain sizes are about 10, 60, and 110μm, respectively. The initial crystallographic texture exhibits basal poles broadly spread along the transverse direction (TD) and the texture intensity was increased with the average grain size.

Quasi-static uniaxial compression and tension test were conducted along the roll direction

(RD) on a Zwick-Z020 testing machine at a strain rate of 1.0×10^{-3} s^{-1}. The samples were deformed up to 0.25 applied strain after which it was prepared for microstructure examination. Another group of samples were tensile to failure in order to character the fracture pattern of samples with various initial grain sizes and diameters. The mechanical test was repeated four times for each condition. Postmortem examination of the fracture surface and texture analysis were performed by using a field emission scanning electron microscope (FE-SEM, FEI Quanta 650, FEI) equipped with an electron backscatter diffraction (EBSD) detector., The samples for EBSD test were cut and ground along the longitudinal section, followed by argon-ion polishing to remove the surface hardening layer. The EBSD results were analyzed by MTEX (Hielscher and Schaeben, 2008), an open source Matlab toolbox for analyzing and modeling crystallographic textures. Since the EBSD test is hard to conduct on the small sample, only the results of samples with D=1.2mm under compression and tension are compared.

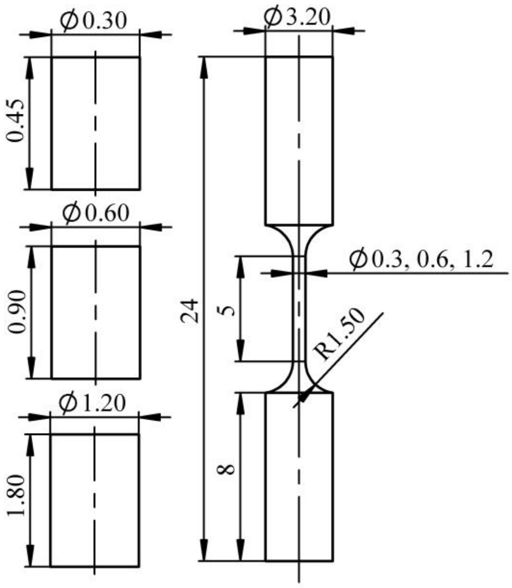

Fig. 1. Dimensions of the compression and tension samples.

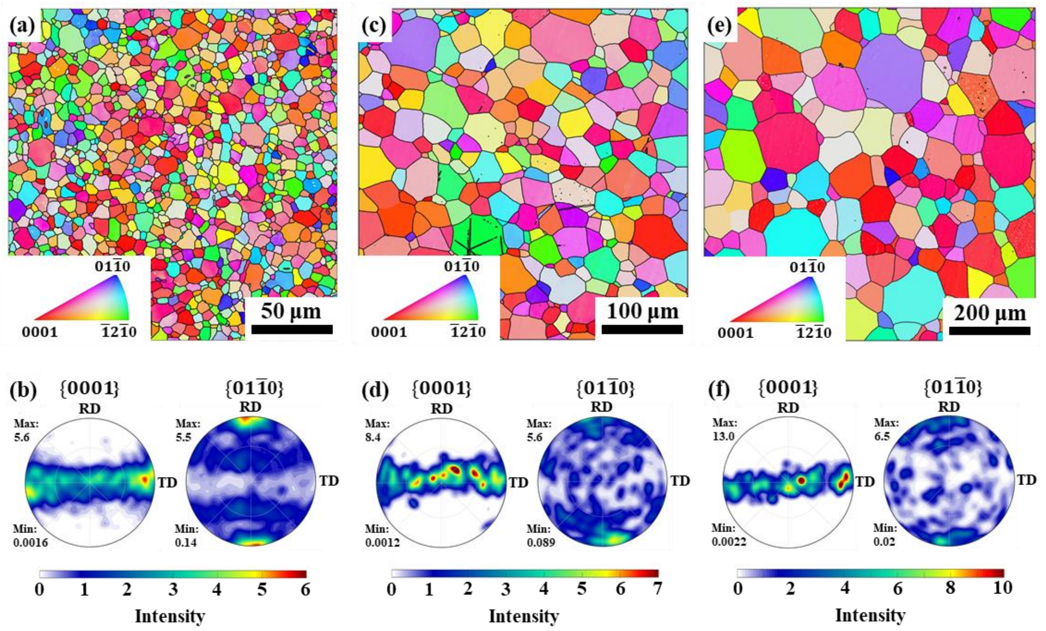

Fig. 2. Microstructure and pole figure of sample treating at 600, 700, and 800°C for 1 h.

3. Modeling methodology

3.1 Mechanism-based non-local crystal plasticity model

A lower-order non-local crystal plasticity model considering dislocation glide and deformation twinning is described in this section. The model is established in the hyperelastic frame.

3.1.1 Crystal plasticity constitutive relations

The total deformation gradient is assumed to admit a multiplicative decomposition as (Asaro and Rice, 1977; Peirce et al., 1982):

$$\mathbf{F}=\mathbf{F}^{e}\mathbf{F}^{p} \tag{1}$$

with $\det\left(\mathbf{F}^{e}\right)>0$ and $\det\left(\mathbf{F}^{p}\right)=1$. Where $\mathbf{F}^{e}=\partial\mathbf{x}/\partial\bar{\mathbf{X}}$ represents the lattice rigid rotation and its elastic distortion, mapping the intermediate configuration ($\bar{\mathbf{X}}$) to the current configuration ($\mathbf{x}$), $\mathbf{F}^{p}=\partial\bar{\mathbf{X}}/\partial\mathbf{X}$ corresponds to the plastic deformation, mapping the initial configuration ($\mathbf{X}$) to the intermediate configuration.

The total velocity gradient $\mathbf{L}$ is divided into elastic ($\mathbf{L}^{e}$) and plastic ($\mathbf{L}^{p}$) parts as:

$$\mathbf{L}=\dot{\mathbf{F}}\mathbf{F}^{-1}=\dot{\mathbf{F}}^{e}\mathbf{F}^{e-1}+\mathbf{F}^{e}\dot{\mathbf{F}}^{p}\mathbf{F}^{p-1}\mathbf{F}^{e-1}=\mathbf{L}^{e}+\mathbf{L}^{p} \tag{2}$$

The plastic velocity gradient $\mathbf{L}^{p}$ due to dislocation glide and deformation twinning is expressed as (Kalidindi, 1998; Ravaji and Joshi, 2021):

$$\mathbf{L}^{\mathrm{p}}=\left(1-\sum_{\beta=1}^{N_{\mathrm{tw}}} f^{\beta}\right) \sum_{\alpha=1}^{N_{\mathrm{s}}} \dot{\gamma}^{\alpha} \mathbf{m}^{\alpha} \otimes \mathbf{n}^{\alpha}+\sum_{\beta=1}^{N_{\mathrm{tw}}} \dot{\gamma}^{\beta} \mathbf{m}^{\beta} \otimes \mathbf{n}^{\beta} \tag{3}$$

where the first and second terms represent the slip and twin in parent, respectively. $\dot{\gamma}$ is the shear strain rate, $\mathbf{m}$ and $\mathbf{n}$ are the direction and plane normal of slip or twinning systems, superscript α and β denote slip and twin mode, respectively. f^{β} is the volume fraction of deformation twin of the twin system β.

The elastic strain is measured with respect to the intermediate configuration, and the elastic response is defined by an elastic stored energy potential w^{e}:

$$w^{\mathrm{e}}=\frac{1}{2} \mathbf{E}^{\mathrm{e}}: \mathbb{R}^{\mathrm{e}}: \mathbf{E}^{\mathrm{e}} \tag{4}$$

where $\mathbb{R}^{\mathrm{e}}$ is the fourth order tensor of elastic moduli, $\mathbf{E}^{\mathrm{e}}=\left(\mathbf{C}^{\mathrm{e}}-\mathbf{I}\right) / 2$ is the elastic Green strain tensor, $\mathbf{C}^{\mathrm{e}}=\mathbf{F}^{\mathrm{eT}} \mathbf{F}^{\mathrm{e}}$ is the elastic right Cauchy-Green strain tensor. The 2nd Piola–Kirchhoff stress $\mathbf{T}^{\mathrm{e}}$ is obtained by:

$$\mathbf{T}^{\mathrm{e}}=\frac{\partial w^{\mathrm{e}}}{\partial \mathbf{E}^{\mathrm{e}}}=\mathbb{R}^{\mathrm{e}}: \mathbf{E}^{\mathrm{e}} \tag{5}$$

The resolved shear stress on a slip system or twinning systems meets:

$$\tau^{\alpha, \beta}=\left(\mathbf{F}^{\mathrm{eT}} \mathbf{F}^{\mathrm{e}} \mathbf{T}^{\mathrm{e}}\right): \mathbf{S}^{\alpha, \beta} \tag{6}$$

where $\mathbf{S}^{\alpha, \beta}=\mathbf{m}^{\alpha, \beta} \otimes \mathbf{n}^{\alpha, \beta}$ is the Schmid factor.

3.1.2 Dislocation glide mediated deformation

Following the thermal activated escape mechanism of dislocation (Kocks et al., 1975; Wu and Curtin, 2015), the contribution to the total shear rate from slip system α is expressed by:

$$\dot{\gamma}^{\alpha}=\dot{\gamma}_0^{\alpha} \exp \left[-\frac{Q_{\mathrm{s}}}{k_{\mathrm{B}} T}\left(1-\left(\frac{\tau^{\alpha}-\tau_{\mathrm{s}}^{\alpha}}{\tau_{*}}\right)^{\mathrm{p}}\right)^{\mathrm{q}}\right] \operatorname{sgn}\left(\tau^{\alpha}\right) \tag{7}$$

where $\dot{\gamma}_0^{\alpha}$ is the reference shear rate, $\tau_{\mathrm{s}}^{\alpha}$ and τ_{*} are the athermal and thermal slip resistance for the α*-th* slip system, respectively. Q_{s} is the activation energy for dislocation slip and k_{B} is the Boltzmann factor. Fitting parameters p and q are set to 1.0 in this paper. The athermal slip resistance, $\tau_{\mathrm{s}}^{\alpha}$, hinders the movement of mobile dislocation on slip system α, which is determined by the interaction between dislocations of coplanar and intersecting slip systems. Splitting the total dislocation into SSD and GND, $\tau_{\mathrm{s}}^{\alpha}$ can be calculated by (Evers, 2004;

Sedaghat and Abdolvand, 2021):

$$\tau_{\mathrm{s}}^{\alpha}=\tau_{\mathrm{i}}^{\alpha}+c_1 G b^{\alpha}\sqrt{\sum_{\alpha'=1}^{N_{\mathrm{s}}}\varsigma^{\alpha\alpha'}\left(\rho_{SSD}^{\alpha'}+\rho_{GND}^{\alpha'}\right)} \tag{8}$$

where $\tau_{\mathrm{i}}^{\alpha}$ is the initial slip resistance, c_1 is a material constant, G is the shear modulus, b is the magnitude of Burgers vector, ρ_{SSD} and ρ_{GND} are the density of SSD and GND, respectively. $\varsigma^{\alpha\alpha'}$ is the hardening matrix between slip system α and α', the value of which is assumed to be 1.0 for coplanar systems and 1.4 for non-coplanar systems.

The evolution of SSD depends on the storage and annihilation process of the same slip system:

$$\rho_{SSD}^{\alpha}=\frac{\left|\dot{\gamma}^{\alpha}\right|}{b^{\alpha}\ell_{\mathrm{s}}^{\alpha}}-\Omega\rho_{SSD}^{\alpha}\left|\dot{\gamma}^{\alpha}\right| \tag{9}$$

where Ω is the parameter for dynamic recovery. The accumulation of SSD is governed by the mean free path for dislocation glide, $\ell_{\mathrm{s}}^{\alpha}$, which is a function of the density of SSD and GND and the volume fraction of deformation twins:

$$\frac{1}{\ell_{\mathrm{s}}^{\alpha}}=\frac{1}{L_{SSD}}\sqrt{\sum_{\alpha'}^{N_{\mathrm{s}}}\varsigma^{\alpha\alpha'}\rho_{SSD}^{\alpha'}}+\frac{1}{L_{GND}}\sqrt{\sum_{\alpha'}^{N_{\mathrm{s}}}\kappa^{\alpha\alpha'}\rho_{GND}^{\alpha'}}+\frac{1}{L_{st}}\sum_{\beta}^{N_{\mathrm{tw}}}\varsigma^{\alpha\beta}f^{\beta}\frac{1}{t_{\mathrm{tw}}(1-f_{\mathrm{tw}})} \tag{10}$$

where L_{SSD}, L_{GND}, and L_{st} are the material constants characterizing the contribution from SSD, GND, and deformation twins, respectively. $\kappa^{\alpha\alpha'}$ is the interaction matrix between the GND of different slip systems, $\varsigma^{\alpha\beta}$ is the interaction matrix between slip system α and twin system β, f^{β} is the volume fraction of twin of system β, t_{tw} and f_{tw} are the mean twin thickness and total twin fraction, respectively.

GND is introduced to maintain the continuity of the lattice. Nye (1953) proposed a dislocation tensor $\mathbf{G}$ to correlate the GND density and plastic deformation gradient. This dislocation tensor has been extended to more rigorous expression by different approaches (Acharya and Bassani, 2000; Busso et al., 2000; Cermelli and Gurtin, 2001). Following (Cermelli and Gurtin, 2001), the net Burger's vector can be calculated by Eq (11) based on the Stokes theorem:

$$\mathbf{B}=\int_{S_0}\left(\mathrm{Curl}\left(\mathbf{F}^{\mathrm{p}}\right)\right)^{\mathrm{T}}\mathbf{n}_0\mathrm{d}A_0=\int_{\bar{S}}\frac{1}{\det\mathbf{F}^{\mathrm{p}}}\left(\mathrm{Curl}\left(\mathbf{F}^{\mathrm{p}}\right)\right)^{\mathrm{T}}\mathbf{F}^{\mathrm{pT}}\bar{\mathbf{n}}\mathrm{d}\bar{A} \tag{11}$$

where $\bar{\mathbf{n}}\mathrm{d}\bar{A}=\left(\det\mathbf{F}^{\mathrm{p}}\right)\mathbf{F}^{\mathrm{p}-\mathrm{T}}\mathbf{n}_0 dA_0$ is the surface element in the intermediate configuration, $\left(1/\det\mathbf{F}^{\mathrm{p}}\right)\left(\mathrm{Curl}\left(\mathbf{F}^{\mathrm{p}}\right)\right)^{\mathrm{T}}\bar{\mathbf{n}}\mathrm{d}\bar{A}$ is the local Burgers vector corresponding to the boundary curve of the surface element. Thus, the geometric dislocation tensor in finite deformation is expressed by (Cermelli and Gurtin, 2001):

$$\mathbf{G}=\frac{1}{\det\mathbf{F}^{\mathrm{p}}}\mathbf{F}^{\mathrm{p}}\mathrm{Curl}\left(\mathbf{F}^{\mathrm{p}}\right) \tag{12}$$

The GND dislocation line can be decomposed in to three components (Busso et al., 2000):

$$\boldsymbol{\rho}_{\mathrm{GND}}^{\alpha}=\rho_{\mathrm{Gs}}^{\alpha}\mathbf{m}^{\alpha}+\rho_{\mathrm{Get}}^{\alpha}\mathbf{t}^{\alpha}+\rho_{\mathrm{Gen}}^{\alpha}\mathbf{n}^{\alpha} \tag{13}$$

where $\rho_{\mathrm{Gs}}^{\alpha}$, is the density of screw components of GND parallel to the slip direction $\mathbf{m}^{\alpha}$, $\rho_{\mathrm{Gen}}^{\alpha}$ and $\rho_{\mathrm{Get}}^{\alpha}$ are the density of edge components of GND parallel to the normal of slip plane $\mathbf{n}^{\alpha}$ and $\mathbf{t}^{\alpha}=\mathbf{m}^{\alpha}\times\mathbf{n}^{\alpha}$, respectively.

Then the relationship between geometric dislocation tensor and the components of GND reads:

$$\mathbf{G}=\sum_{\alpha=1}^{N_{\mathrm{s}}}\left(\rho_{\mathrm{Gs}}^{\alpha}\mathbf{b}^{\alpha}\otimes\mathbf{m}^{\alpha}+\rho_{\mathrm{Get}}^{\alpha}\mathbf{b}^{\alpha}\otimes\mathbf{t}^{\alpha}+\rho_{\mathrm{Gen}}^{\alpha}\mathbf{b}^{\alpha}\otimes\mathbf{n}^{\alpha}\right) \tag{14}$$

The density of the components of GND could be solved by using L_2 minimization method proposed by Arsenlis and Parks (1999):

$$\left\{\rho_{\mathrm{GND}}^{\alpha}\right\}=\mathbf{A}^{\mathrm{T}}(\mathbf{A}\mathbf{A}^{\mathrm{T}})^{-1}\hat{\mathbf{G}} \tag{15}$$

where $\left\{\rho_{\mathrm{GND}}^{\alpha}\right\}$ is $3N_{\mathrm{s}}\times1$ vector containing the edge and screw components of GND of slip system α, $\mathbf{A}$ is a $9\times3N_{\mathrm{s}}$ matrix consists of the basis tensor $\mathbf{b}^{\alpha}\otimes\mathbf{m}^{\alpha}$, $\mathbf{b}^{\alpha}\otimes\mathbf{t}^{\alpha}$, and $\mathbf{b}^{\alpha}\otimes\mathbf{n}^{\alpha}$, $\hat{\mathbf{G}}$ is the vector form of geometric dislocation tensor $\mathbf{G}$ with a dimension of 9×1. The total GND density of slip system α is defined as:

$$\rho_{\mathrm{GND}}^{\alpha}=\sqrt{\left(\rho_{\mathrm{Gs}}^{\alpha}\right)^{2}+\left(\rho_{\mathrm{Get}}^{\alpha}\right)^{2}+\left(\rho_{\mathrm{Gen}}^{\alpha}\right)^{2}} \tag{16}$$

3.1.3 Deformation twinning

The nucleation and propagation of deformation twin are follow the model proposed by (Tang et al., 2019; Wong et al., 2016). The nucleation rate of twin system β is

$$\dot{N}^{\beta}=\dot{N}_{0}^{\beta}p_{\mathrm{nsc}}p_{\mathrm{tw}}^{\beta} \tag{17}$$

where $\dot{N}_{0}^{\beta}$ is the number density of potential twin nuclei per unit time. The probability that cross-slip does not occur, p_{nsc}, is assumed to be 1.0. p_{tw}^{β} is the probability that twin nucleus bows out to form a twin and is given as:

$$p_{\mathrm{tw}}^{\beta}=\exp\left(-\left(\frac{\tau_{\mathrm{c}}^{\beta}}{\tau^{\beta}}\right)^{\mathrm{r}}\right) \tag{18}$$

where τ^{β} is the resolved shear stress on twin system β, τ_c^{β} is the critical stress for twinning that meets the Hall-Petch relation with grain size:

$$\tau_c^{\beta}=\tau_0^{\beta}+K_{\mathrm{tw}}^{\beta}\Big/\sqrt{d} \tag{19}$$

where τ_0^{β} is a parameter related to the stacking fault energy (Sun et al., 2018).

The volume of deformation twins of twinning system evolves as:

$$f^{\beta}=\left(1-\sum_{\beta=1}^{N_{\mathrm{tw}}}f^{\beta}\right)V^{\beta}\dot{N}^{\beta} \tag{20}$$

where V^{β} is the volume of a new twin:

$$V^{\beta}=\frac{\pi}{4}\ell_{\mathrm{tw}}^{2}t_{\mathrm{tw}} \tag{21}$$

The mean free path for deformation twinning, ℓ_{tw}, is expressed as:

$$\frac{1}{\ell_{tw}}=\frac{1}{L_{tw}}\left(\frac{1}{d}+\sum_{\beta=1}^{N_{tw}}\varsigma^{\beta\beta'}f^{\beta'}\frac{1}{t_{tw}(1-f_{tw})}\right) \tag{22}$$

where L_{tw} is a fitting parameter, $\varsigma^{\beta\beta'}$ is the interaction matrix between two different twin system β and β'.

The shear strain rate for twin system β is calculated as (Hosford, 1993; Kalidindi, 1998):

$$\dot{\gamma}^{\beta}=\gamma_{\mathrm{tw}}\dot{f}^{\beta} \tag{23}$$

where γ_{tw} is the characteristic shear strain for deformation twinning, which is a function of lattice constant:

$$\gamma_{tw}=\begin{cases}\dfrac{\sqrt{3}}{(c/a)}-\dfrac{(c/a)}{\sqrt{3}} & \{1\,0\,\bar{1}\,2\}\langle 1\,0\,\bar{1}\,\bar{1}\rangle \\[2ex] \dfrac{2\left((c/a)^{2}-2\right)}{3(c/a)} & \{1\,1\,\bar{2}\,2\}\langle 1\,1\,\bar{2}\,\bar{3}\rangle\end{cases} \tag{24}$$

where $c/a=1.587$ for titanium.

Deformation twin cause abrupt lattice reorientation when the twin fraction exceeds a threshold value f_{th}^{β}. The rotation matrix for rotating the crystal frame about the twin plane is (Houtte, 1978):

$$\mathbf{R}^{\mathrm{tw}}=2\mathbf{n}^{\beta}\otimes\mathbf{n}^{\beta}-\mathbf{I} \tag{25}$$

where $\mathbf{n}^{\beta}$ represents the plane normal of twin system β, $\mathbf{I}$ is the identity tensor.

3.2 Numerical implementation

This non-local crystal plasticity model was implemented into Abaqus/Explicit via VUMAT where the stress was computed on the corotational coordinate system. To avoid unnecessary rotation of tensors defined in the lattice coordinate system and to introduce the size effect on the yield point, $\mathbf{F}^{\mathrm{p}}$ was initialized by the initial crystal orientation $\mathbf{Q}_0$ (Ma et al., 2006). The computational framework performed within a single time step is shown in Table 1. Noted that the right stretch tensor $\mathbf{U}$ was used instead of deformation gradient $\mathbf{F}$ since the rigid rotation was not performed on the corotational coordinate system. A element-free Galerkin method was employed to calculate $\mathrm{Curl}\left(\mathbf{F}^{\mathrm{p}}\right)$ of a integration point (IP) according to its neighborhood (Belyschko et al., 1996; Zhang and Dong, 2015). According to the moving least squares approximation, the object function $u(\mathbf{x})$ could be approximated by $\tilde{u}(\mathbf{x})$ as:

$$\tilde{u}(\mathbf{x})=\sum_{i=1}^{n} p_i(\mathbf{x})a_i(\mathbf{x})=\mathbf{p}^{\mathrm{T}}(\mathbf{x})\mathbf{a}(\mathbf{x}) \tag{26}$$

where n is the dimension of basis function $\mathbf{p}(\mathbf{x})$, $\mathbf{a}(\mathbf{x})$ is the vector of undetermined coefficient which is computed by its coordinate $\mathbf{x}$. The bi-linearity basis function was used in this work:

$$\mathbf{p}=[1,x,y,z,xy,yz,zx]^{\mathrm{T}},\ \text{with } n=7 \tag{27}$$

The coefficient vector $\mathbf{a}(\mathbf{x})$ can be determined by minimizing the following function:

$$L=[\mathbf{Pa}-\mathbf{u}]^{\mathrm{T}}\mathbf{W}[\mathbf{Pa}-\mathbf{u}] \tag{28}$$

where $\mathbf{P}$ is a $N\times n$ matrix consist of the basis function for N IPs within the influence domain of the considered IP, $\mathbf{W}=\mathrm{diag}(w(\mathbf{x},\mathbf{x}_1),w(\mathbf{x},\mathbf{x}_2),\cdots w(\mathbf{x},\mathbf{x}_N))$ with $w(\mathbf{x},\mathbf{x}_{\mathrm{I}})=w(r_x)w(r_y)w(r_z)$, where $w(r)$ is the weight function for neighbor IPs $\mathbf{x}_{\mathrm{I}}$ belong to the influence region of considered IP $\mathbf{x}$, which reads:

$$w(r)=\begin{cases} 2/3-4r^2+4r^3 & r\leqslant 0.5 \\ 4/3-4r+r^2-4/3r^3 & 0.5\leqslant r\leqslant 1 \\ 0 & r>1 \end{cases} \tag{29}$$

where $r=\|\mathbf{x}-\mathbf{x}_{\mathrm{I}}\|$, is the distance between considered IP and its neighbor IPs. The cube influence domain with size of D is used in this work, i.e., $r_x=|x-x_{\mathrm{I}}|/D$, $r_y=|y-y_{\mathrm{I}}|/D$, $r_z=|z-z_{\mathrm{I}}|/D$.

The minimizing solution of Eq. (28) is:

$$\mathbf{a}(\mathbf{x})=\mathbf{A}^{-1}(\mathbf{x})\mathbf{B}(\mathbf{x})\mathbf{u} \tag{30}$$

where $\mathbf{A}(\mathbf{x})=\mathbf{P}^{\mathrm{T}}\mathbf{W}(\mathbf{x})\mathbf{P}$ and $\mathbf{B}(\mathbf{x})=\mathbf{P}^{\mathrm{T}}\mathbf{W}(\mathbf{x})$. Substitute the above equation into Eq. (26), $\tilde{u}(\mathbf{x})$ is expressed by:

$$\tilde{u}(\mathbf{x})=\sum_{i=1}^{N}\Phi_{\mathrm{I}}(\mathbf{x})u\left({}^{\mathrm{I}}\mathbf{x}\right)=\boldsymbol{\Phi}^{\mathrm{T}}(\mathbf{x})\mathbf{u} \tag{31}$$

$$\boldsymbol{\Phi}^{\mathrm{T}}(\mathbf{x})=[\Phi_1(\mathbf{x}),\Phi_2(\mathbf{x}),\cdots,\Phi_N(\mathbf{x})]=\mathbf{p}^{\mathrm{T}}(\mathbf{x})\mathbf{A}^{-1}(\mathbf{x})\mathbf{B}(\mathbf{x}) \tag{32}$$

where $\boldsymbol{\Phi}(\mathbf{x})$ the vector of shape function. By using Eq. (31), the derivatives of the plastic deformation gradient at each IP can be computed as:

$$\frac{\partial F_{ij}^{\mathrm{p}}}{\partial x_k}=\sum_{\mathrm{I}=1}^{N}\frac{\partial \Phi_{\mathrm{I}}}{\partial x_k}\,{}^{\mathrm{I}}F_{ij}^{\mathrm{p}} \tag{33}$$

Finally, the curl of plastic deformation gradient can be obtained:

$$\left(\mathrm{Curl}\left(\mathbf{F}^{\mathrm{p}}\right)\right)_{ij}=\epsilon_{ipq}\frac{\partial F_{jq}^{\mathrm{p}}}{\partial x_p} \tag{34}$$

where ϵ_{ipq} is the permutation tensor.

Table1 Computational framework of the non-local CPFE model.

```
0  Initialize state variables: $\mathbf{Q}_0$, $\mathbf{F}^{\mathrm{p}}=\mathbf{Q}_0$, $\mathbf{m}_0$, $\mathbf{n}_0$ and $\rho_{\mathrm{SSD},0}^{\alpha}$, etc.
1  Read the known variables: $\mathbf{U}_{\mathrm{n}}$, $\mathbf{U}_{\mathrm{n+1}}$, $\mathbf{F}_{\mathrm{n}}^{\mathrm{p}}$, $\mathbf{m}_{\mathrm{n}}$, $\mathbf{n}_{\mathrm{n}}$, $f_{\mathrm{n}}^{\beta}$ and $\rho_{\mathrm{SSD,n}}^{\alpha}$.
2  Compute the total twin fraction for each twin system: $f_{\mathrm{n}}^{\mathrm{C}}$, $f_{\mathrm{n}}^{\mathrm{T}}$.
   if $f_{\mathrm{n}}^{\mathrm{C}}$, $f_{\mathrm{n}}^{\mathrm{T}}>f_{\mathrm{th}}$ then
3      Find the rotation matrix $\mathbf{R}_{\mathrm{n}}^{\mathrm{tw}}=2\mathbf{n}_{\mathrm{n}}^{\beta}\otimes\mathbf{n}_{\mathrm{n}}^{\beta}-\mathbf{I}$.
4      Rotate the slip and twinning vector: $\mathbf{m}_{\mathrm{n+1}}^{\alpha,\beta}=\mathbf{R}_{\mathrm{n}}^{\mathrm{tw}}\mathbf{m}_{\mathrm{n}}^{\alpha,\beta}$, $\mathbf{n}_{\mathrm{n+1}}^{\alpha,\beta}=\mathbf{R}_{\mathrm{n}}^{\mathrm{tw}}\mathbf{n}_{\mathrm{n}}^{\alpha,\beta}$.
   end if
5  Compute $\rho_{\mathrm{GND}}^{\alpha}$ using the element-free Galerkin method:
   (a) Search the influence region and compute the shape function $\Phi_{\mathrm{I}}$ using Eq. (32).
   (b) Calculate the curl of $\mathbf{F}_{\mathrm{n}}^{\mathrm{p}}$ using Eqs. (33)-(34).
   (c) Compute the dislocation tensor $\mathbf{G}_{\mathrm{n+1}}=\mathbf{F}_{\mathrm{n}}^{\mathrm{p}}\mathrm{Curl}\left(\mathbf{F}_{\mathrm{n}}^{\mathrm{p}}\right)$
   (d) Construct matrix $\mathbf{A}_{\mathrm{n+1}}$ using $\mathbf{b}_{\mathrm{n+1}}^{\alpha}\otimes\mathbf{m}_{\mathrm{n+1}}^{\alpha}$, $\mathbf{b}_{\mathrm{n+1}}^{\alpha}\otimes\mathbf{t}_{\mathrm{n+1}}^{\alpha}$, and $\mathbf{b}_{\mathrm{n+1}}^{\alpha}\otimes\mathbf{n}_{\mathrm{n+1}}^{\alpha}$.
   (e) Update the components of GND and the total GND density using Eqs. (15)-(16).
6  Calculate the resolved shear stress: $\tau_n^{\alpha,\beta}=(\mathbf{F}_{\mathrm{n}}^{\mathrm{eT}}\mathbf{F}_{\mathrm{n}}^{\mathrm{e}}\mathbf{T}_{\mathrm{n}}^{\mathrm{e}}):\mathbf{S}_{\mathrm{n+1}}^{\alpha,\beta}$.
```

```
7  Compute $\mathbf{L}_{\mathrm{n}}^{\mathrm{p}}$ using Eq. (3) and update $\mathbf{F}^{\mathrm{p}}$: $\mathbf{F}_{\mathrm{n+1}}^{\mathrm{p}} = (\mathbf{I} + \Delta t\,\mathbf{L}_{\mathrm{n}}^{\mathrm{p}})\mathbf{F}_{\mathrm{n}}^{\mathrm{p}}$.
8  Normalize the plastic deformation gradient: $\mathbf{F}_{\mathrm{n+1}}^{\mathrm{p}} = \dfrac{\mathbf{F}_{\mathrm{n+1}}^{\mathrm{p}}}{\sqrt[3]{\det(\mathbf{F}_{\mathrm{n+1}}^{\mathrm{p}})}}$
9  Update slip/twinning rate, shear strain, and resistance using Eqs. (7)-(8).
10 Find the elastic deformation gradient: $\mathbf{F}_{\mathrm{n+1}}^{\mathrm{e}} = \mathbf{U}_{\mathrm{n+1}}\mathbf{F}_{\mathrm{n+1}}^{\mathrm{p}-1}$
11 Compute $\mathbf{E}^{\mathrm{e}}$ and $\mathbf{T}^{\mathrm{e}}$: $\mathbf{E}_{\mathrm{n+1}}^{\mathrm{e}} = (\mathbf{F}_{\mathrm{n+1}}^{\mathrm{eT}}\mathbf{F}_{\mathrm{n+1}}^{\mathrm{e}} - \mathbf{I})/2$, $\mathbf{T}_{\mathrm{n+1}}^{\mathrm{e}} = \mathbb{R}^{\mathrm{e}}:\mathbf{E}_{\mathrm{n+1}}^{\mathrm{e}}$.
12 Update the Cauchy stress: $\boldsymbol{\sigma}_{\mathrm{n+1}} = \dfrac{1}{\det(\mathbf{F}_{\mathrm{n+1}}^{\mathrm{e}})}\mathbf{F}_{\mathrm{n+1}}^{\mathrm{e}}\mathbf{T}_{\mathrm{n+1}}^{\mathrm{e}}\mathbf{F}_{\mathrm{n+1}}^{\mathrm{eT}}$.
13 Calculate the rigid rotation matrix: $\mathbf{R}_{\mathrm{n+1}}^{\mathrm{e}} = \mathbf{F}_{\mathrm{n+1}}^{\mathrm{e}}\mathbf{U}_{\mathrm{n+1}}^{\mathrm{e}-1}$.
14 Output the crystal orientation matrix:
   if $f_{\mathrm{n}}^{\mathrm{C}}$, $f_{\mathrm{n}}^{\mathrm{T}} > f_{\mathrm{th}}$ then
       $\mathbf{Q}_{\mathrm{n+1}} = \mathbf{R}_{\mathrm{n+1}}^{\mathrm{tw}}\mathbf{R}_{\mathrm{n+1}}^{\mathrm{eT}}$      ($\mathbf{Q}_0$ is omitted since $\mathbf{F}^{\mathrm{p}}$ is initialized by $\mathbf{Q}_0$)
   else
       $\mathbf{Q}_{\mathrm{n+1}} = \mathbf{R}_{\mathrm{n+1}}^{\mathrm{eT}}$
   end if
```

3.3 Representative volume elements and model calibration

Cylindrical representative volume elements (RVEs) with the same diameter and similar grain size to the experiment were used to calibrate the non-local crystal plasticity model and study the size effect affected T-C asymmetry and plastic heterogeneity, as shown in Fig. 3. To reduce the computational cost, the geometric models of the samples with d=10μm, D=0.3mm and d=110μm, D=1.2mm were simplified into 1/8 model based on their symmetry planes. The C3D8R element with size of ~2.0μm was utilized to discrete the cylinder. The initial Euler angle in Bunge convention of each grain was extracted from the corresponding EBSD result. Uniaxial tension and compression in microscale were performed to identify the material parameters and investigate size-dependent plastic asymmetry and heterogeneity. Considering the fracture strain of small sample ($d \le$ 0.6mm) in the tensile test may be lower than 0.25. Another set of simulations with different grain sizes under the diameter of 1.2mm was performed to verify the predicted asymmetrical texture evolution by comparing it with experimental results. In these simulations, cubic RVEs with periodic boundary conditions were utilized as the full-field simulation under natural boundary conditions is unlikely conducted when D=1.2 and $d \le$ 60μm.

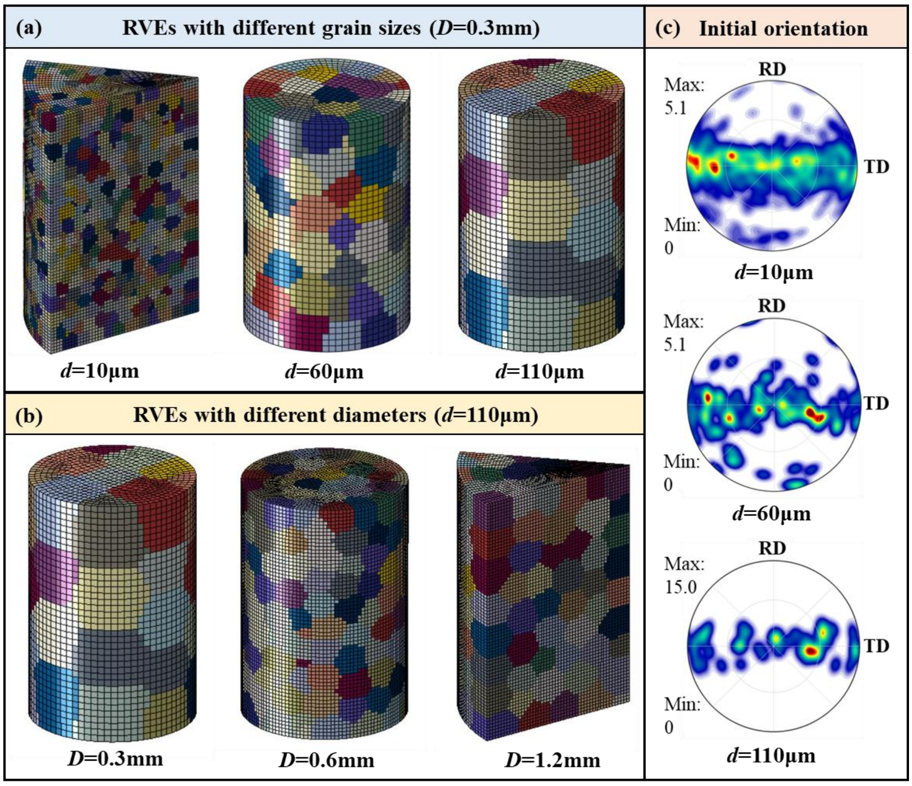

Fig. 3. RVEs and initial crystallographic orientation for the full-field simulation: (a) RVEs with different grain sizes, (b) RVEs with different diameters, and (c) initial orientation for various grain sizes.

In this research, four slip systems and two twinning systems were activated in the simulation. They are three $\{1\bar{1}00\}<11\bar{2}0>$ prismatic <**a**>, three $\{0001\}<11\bar{2}0>$ basal <**a**>, six $\{1\bar{1}01\}<11\bar{2}0>$ pyramidal <**a**>, and twelve $\{10\bar{1}1\}<11\bar{2}3>$ pyramidal <**c**+**a**> slip systems sorted by CRSS in ascending order (Warwick et al., 2012). $\{10\bar{1}2\}<10\bar{1}\bar{1}>$ tension (T1) twin and $\{11\bar{2}2\}<11\bar{2}\bar{3}>$ contraction (C1) twin were included according to experimental evidence (Kumar et al., 2018; Tang et al., 2019). Single crystal elastic constants of CP-Ti are C_{11}=160.0GPa, C_{12}=90.0GPa, C_{13}=66.0GPa, C_{33}=181.0GPa, and C_{44}=46.5 GPa (Levy et al., 2001). Other material parameters were inversely identified from the experimental stress-strain curves and pole figures, as listed in Tables 2 and 3. The ratios of τ_{i}^{α} with respect to prismatic <**a**> of basal <**a**>, pyramidal <**a**> and pyramidal <**c**+**a**> slip modes are 1.80, 2.12, and 2.83, respectively.

Table 2. Dislocation slip relevant material parameters.

Parameter	**prismatic**	**basal**	**pyramidal<a>**	**pyramidal<c+a>**
$\dot{\gamma}_0^\alpha$ (s^{-1})	0.001	0.001	0.001	0.001
Q_s (J)	1.2×10^{-19}	1.2×10^{-19}	1.2×10^{-19}	1.2×10^{-19}
τ_* (MPa)	10.0	10.0	10.0	10.0
p	1.0	1.0	1.0	1.0
q	1.0	1.0	1.0	1.0
c_1	7.2×10^{-3}	7.2×10^{-3}	7.2×10^{-3}	7.2×10^{-3}
b^α (m)	2.95×10^{-10}	2.95×10^{-10}	2.95×10^{-10}	5.53×10^{-10}
τ_i^α (MPa)	34.0	61.2	72.0	96.3
Ω	40.0	40.0	40.0	40.0
L_{SSD}	0.49	0.49	0.49	0.49
L_{GND}	0.06	0.06	0.06	0.06
L_{st}	2.2×10^{-4}	2.2×10^{-4}	2.2×10^{-4}	2.2×10^{-4}

Table 2. deformation twinning relevant material parameters.

Twin system	t_{tw} (m)	L_{tw}	$\dot{N}_0^\beta$	τ_0^β (MPa)	K_tw^β	r
$\{10\bar{1}2\}<10\bar{1}\bar{1}>$	3.5×10^{-6}	0.5	1.5×10^{15}	45.0	2.4×10^{4}	8.0
$\{11\bar{2}2\}<11\bar{2}\bar{3}>$	3.5×10^{-6}	1.0	1.5×10^{15}	130.0	1.8×10^{6}	8.0

4. Results and discussion

4.1 Mechanical response and microstructure

The experimental and simulated stress-strain curves are compared in Fig. 4. The predictions are consistent with the experimental results. Effect of grain size on the asymmetric mechanical response is captured by the non-local crystal plasticity model, as shown in Fig. 4a-b. The predicted stresses are lower than the experimental one without considering the additional hardening provided by the GND. Moreover, the effect of grain size is weakened when excludes the role of GND. It verifies that the crystallographic misorientation cannot sufficiently reflect the effect of GBs (Ma et al., 2006; Zhang et al., 2018). Sigmoidal hardening is observed in the compression curves (Fig. 4b) and it becomes more obvious with the increase of grain size, which is governed by the formation of twins and corresponding reorientation (Habib et al., 2017; Yang et al., 2020; Zecevic et al., 2017). From Fig. 4a, it is found that the simulated tensile stress of the specimen with d=110μm also shows a less obvious secondary hardening after the true strain exceeds 0.2. But stress-strain curve of the specimen with d≤60μm shows no secondary hardening. This is because the deformation twinning is easier to activate at the coarse grain and brings about additional obstruction for dislocation movement (Kumar et al., 2018; Tang et al., 2019). The sigmoidal hardening is still presented for the predicted stress without GND, while the inflection point moves rearward. The lower stress delays the nucleation and growth of deformation twin (Eq. (17)), resulting in the belated secondary hardening. The sigmoidal hardening causes an increase in true stress and results in more severe T-C asymmetry after yielding.

An interesting finding is that the compression stress of the specimen with d=110μm and D=0.3mm overtakes that of the specimen with d=60μm and D=0.3mm, breaking the traditional dependence of stress on grain size (Fig. 4b). It should be noted that this phenomenon is not observed in the specimen that the diameter is larger than 0.3mm. When excluding the effect of GND, this phenomenon becomes more obvious. The compressive stress-strain curves intersect with each other and exhibit an inverse law when strain exceeds 0.15 (Fig. 4b). Since the GND density of fine-grained sample calculated by the non-local model is high (Fig. 18), the stress drops more in the specimen with fine grains when GND is excluded. Consequently, the critical stress for activating deformation twinning will be reached at a larger strain, resulting in a lower strain hardening rate.

The effect of diameter on mechanical response is shown in Fig. 4c-d. Both the experimental and simulated results indicate that the tensile stress is decreased with diameter (Fig. 4c), which is consistent with previous researches (Fu and Chan, 2011). However, the experimental compressive stresses of different diameters are very close, which may be attributed to the size-affected friction. (Fu et al., 2016; Guo et al., 2010) found that the friction coefficient is increased with miniaturization of part. The decreasing tendency is then compensated by the increasing friction.

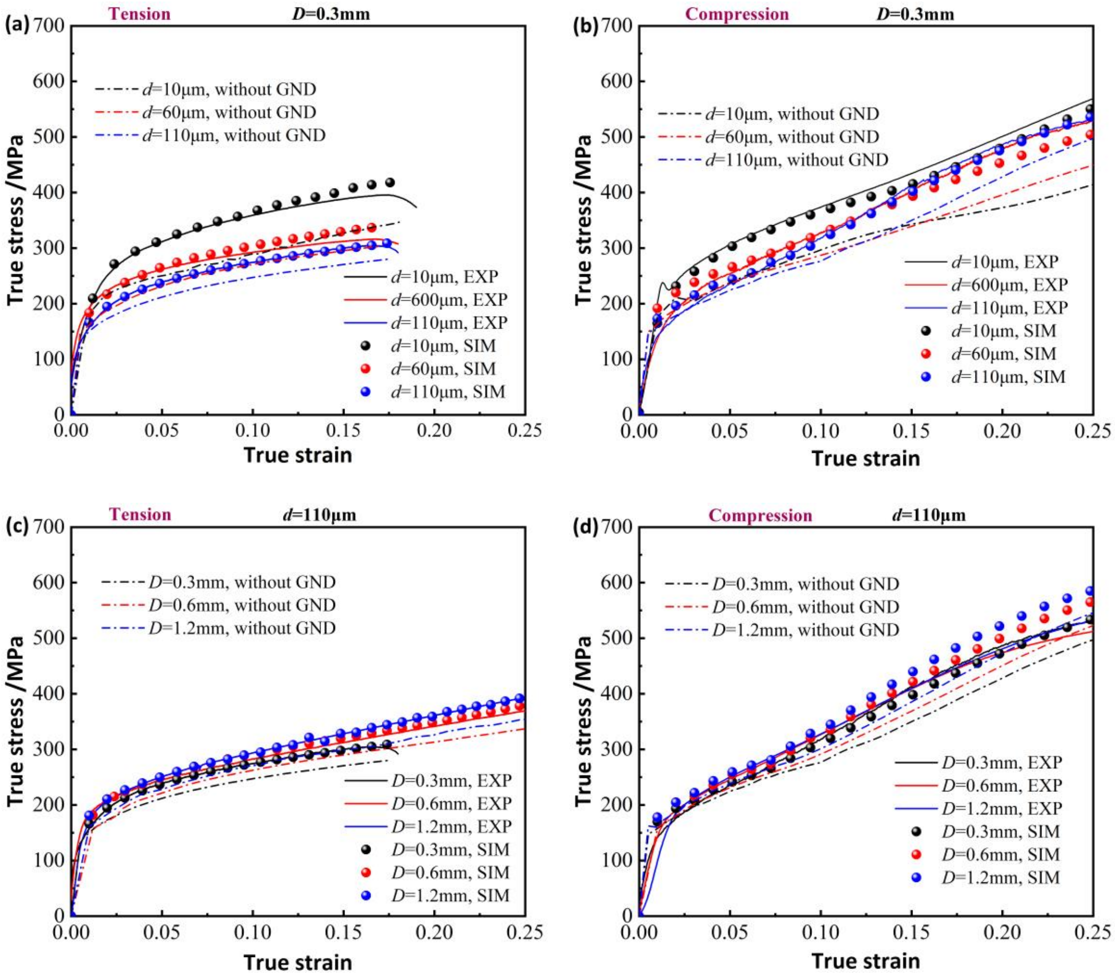

Fig. 4. Comparisons of experimental (solid lines) and predicted (symbols) stress-strain curves. (a) effect of grain size on tensile stress, (b) effect of grain size on compressive stress, (c) effect of diameter on tensile stress, and (d) effect of diameter on compressive stress. Dash dot line represents the predicted value without considering GND.

To quantitatively evaluate the T-C asymmetry, the true stress ratio, compressive true stress (CTS)/tensile true stress (TTS), is plotted in Fig. 5. The CTS/TTS at the initial yielding point is very close to 1.0, regardless of grain size and diameter, indicating very weak T-C asymmetry of CP-Ti in yielding strength. This is consistent with the observations reported in prior works (Baral et al., 2018; Nixon et al., 2010; Suryawanshi et al., 2021). The CTS/TTS generally increases with strain and grain size since more prevailing deformation twins are activated under compression, leading to a higher strain hardening rate. There is no apparent discrepancy in CTS/TTS at low strain under different diameters. When $\varepsilon \geqslant 0.15$, it is found that the CTS/TTS is increased with the reducing diameter. This phenomenon may be caused by the asymmetrical dependency of slip and twinning activity on diameter, which will be analyzed in the next section. Without considering the GND effect (the dashed line in Fig. 5), the simulated CTS/TTS is reduced, especially in the fine-grained sample. Therefore, the T-C asymmetry is enhanced with the increasing grain size and the decreasing diameter of specimen.

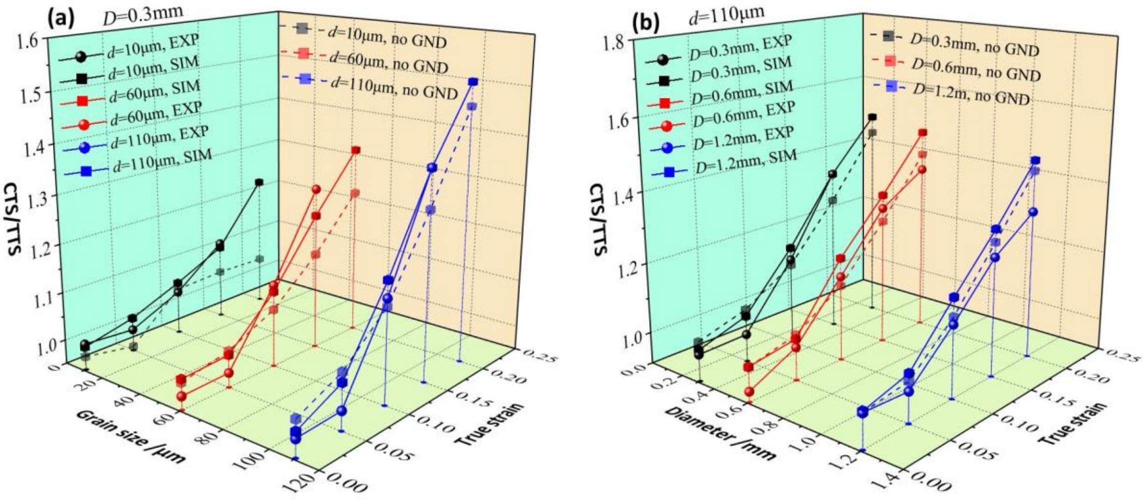

Fig. 5. Evolution of CTS/TTS with strain under different (a) grain sizes and (b) diameters.

Fig. 6 illustrates the band contrast map and corresponding (0001) pole figure of the specimen with *D*=1.2mm and different grain sizes after straining to 0.25. Twin boundaries (TBs) with special misorientation angles are delineated by colored lines. The red and blue TBs are characterized by angle/axes of ~85°/<11-20> and ~65°/<10-10>, which are coincident with boundary characteristics of T1 and C1 twin, respectively. It is found that most deformation twins belong to these two types of twin modes. The number of twin lamellae increases distinctly with initial grain size regardless of the loading direction. More prevalent twins are generated in the compressed specimen than in the tensile counterpart. Some deformation twins are observed even in the specimen with *d*=10μm (Fig. 6d). These twins reduce the mean free path for dislocation glide, cause secondary hardening (Fig. 4), and enhance the T/C asymmetry with increasing grain size (Fig. 5).

The (0001) pole figure changes slightly under tension of fine-grained specimen (Fig. 6a), whereas new texture component having the c-axis oriented to RD with a variation of ≤45° appears under the compression mode (Fig. 6d). This new texture component stems from twinning induced reorientation and it becomes more intensified with the increase of grain size due to the more pronounced twin activities (Fig. 6e-f). The (0001) pole figure of the specimen with *d*≥60μm also has the texture component <c> //RD although the intensity is lower than the compression one. The newly generated texture weakens the initial basal texture in Fig. 2 and this twinning induced reorientation was essentially reproduced by the simulation. Because the RVEs of coarse grain only have several dozen grains the simulated texture intensity of specimen with *d*≥60μm is higher than the experimental one.

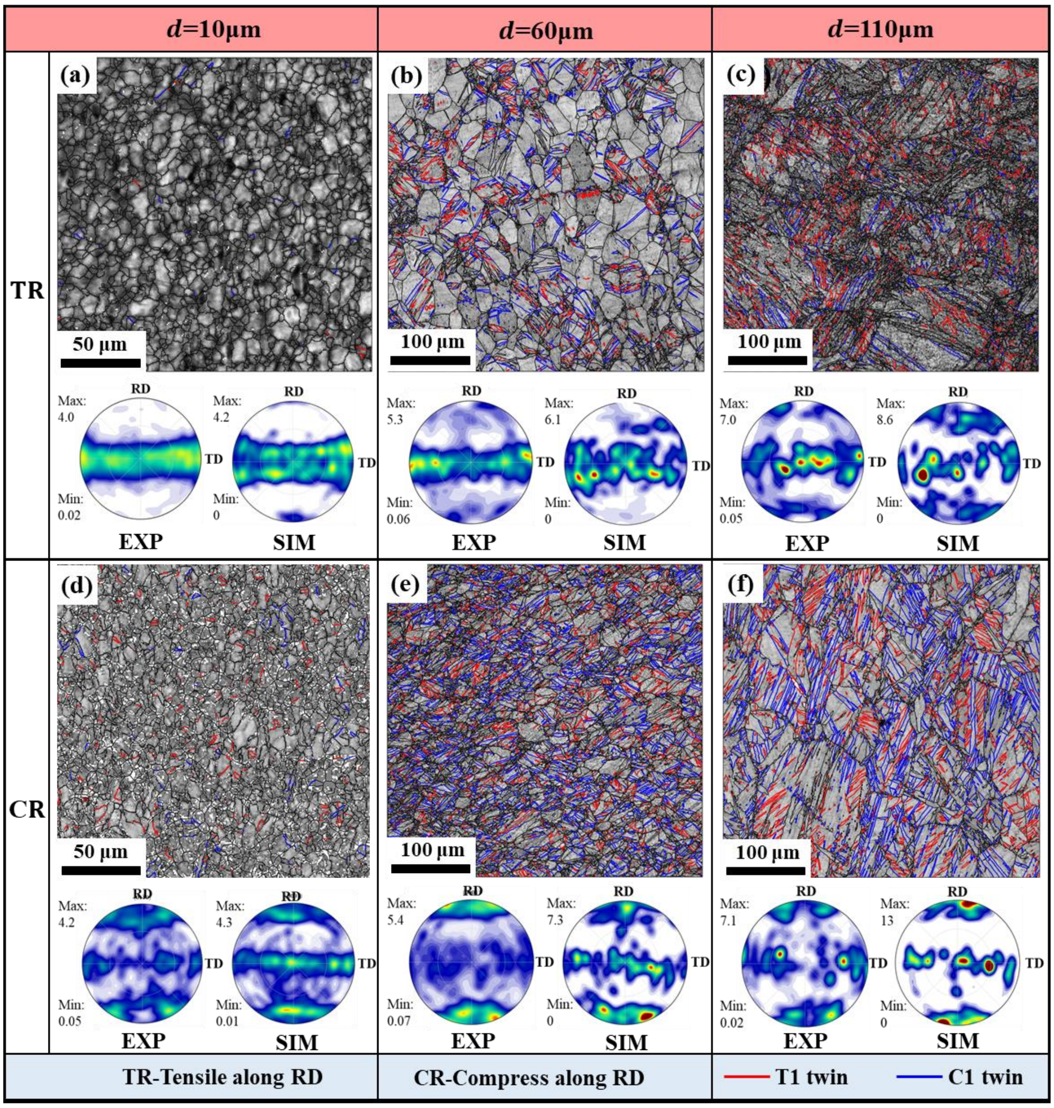

Fig. 6. Effect of grain size and loading direction on the deformed microstructures. (a) d=8μm, tension, (b) d=60μm, tension, (c) d=110μm, tension, (d) d=8μm, compression, (e) d=60μm, compression, and (f) d=110μm, compression.

4.2 Slip and twinning activity

The evolution of relative activity of slip/twinning system is utilized to analyze the underlying mechanism for the size-dependent asymmetric mechanical response. The relative activity for each slip/twinning family at an integration point is characterized by (Tomé et al., 1991):

$$r^{\alpha} = \frac{\sum_{i=1}^{n} \left| \Delta \gamma_i^{\alpha} \right|}{\sum_{\alpha=1}^{m} \sum_{i=1}^{n} \left| \Delta \gamma_i^{\alpha} \right|} \tag{35}$$

where m is the number of slip/twinning family and n is the number of slip/twinning variants of family α.

Fig. 7 shows the effect of grain size on the average slip/twinning activity under tension/compression. The dash dot line represents the result without considering the effect of GND. For all the deformation conditions, the prismatic slip accommodates the most plastic deformation in the early stage of tension and compression due to its lowest CRSS. After the activation of other slip systems, the relative activity of prismatic slip gradually reduces to a relatively stable stage. The tensile deformation is dominated by prismatic slip over the entire strain range under all the grain size conditions. Especially in the tension of fine-grained specimen (Fig. 7a), the relative activity remains stable after the activation of basal, pyramidal<a>, and pyramidal <c+a> slip, and the contribution from deformation twinning is negligible, which is consistent with the result of (Wronski et al., 2018). In compression of fine-grained specimen (Fig. 7b), however, T1 twin is activated at early stage and the relative activity of pyramidal<c+a> and basal slip increase again accompanied by the decreased activity of prismatic slip and T1 twin (Knezevic et al., 2013; Yang et al., 2020; Zecevic et al., 2017). This is caused by the twinning induced reorientation where the favorable slip modes in the reoriented grains are pyramidal<c+a> and basal slip. Meanwhile, the increasing pyramidal<c+a> and basal slip activity lead to the secondary hardening (Fig. 4) due to their higher CRSS than prismatic slip.

With the increase of grain size, the relative activity of T1 twin in compression increases more quickly at low strain. It causes the fronted inflection point for the increasing pyramidal<c+a> and basal slip (Fig. 7d, f). In the tension of specimen with d=110μm, the C1 twin is activated and leads to increased basal slip activity and decreased prismatic slip activity (Fig. 7e). It further causes the secondary hardening after strain exceeds ~0.2 as shown in Fig .4a, c. The difference in the activity of pyramidal<c+a> and basal slip, and T1 twin between tension and compression is increased with grain size, which is responsible for the enhanced T-C asymmetry in the coarse-grained specimen. Since the initial texture of the fine-grained specimen is much weaker than that of coarse grain one (Fig. 2), it has more favorable orientation for the activation of pyramidal<c+a> and basal slip. In contrast, the activatable slip system is limited in the coarse-grained specimen because it consists of several dozen grains with severe texture (Fig. 3). As a result, the relative activity of prismatic slip is increased with grain size in the tensile deformation before twinning induced reorientation occupies a certain proportion, as shown in Fig. 7a, c ,e. Namely, the other slip mode is hard to be activated in the coarse-grained specimen. This phenomenon is also attributed to the enhanced T-C asymmetry under the coarse-grained specimen.

When GND is excluded (dash dot line in Fig. 7), it is found that the prismatic slip becomes more dominated. Twin activity is slow down and the relative activities of pyramidal<c+a> and basal slip are decreased. The effect of GND on slip/twinning activity is more significant in the compression deformation and the difference in slip/twinning activity between tension and compression is decreased. This is why the predicated T-C asymmetry is reduced when excluding the role of GND (Fig. 5).

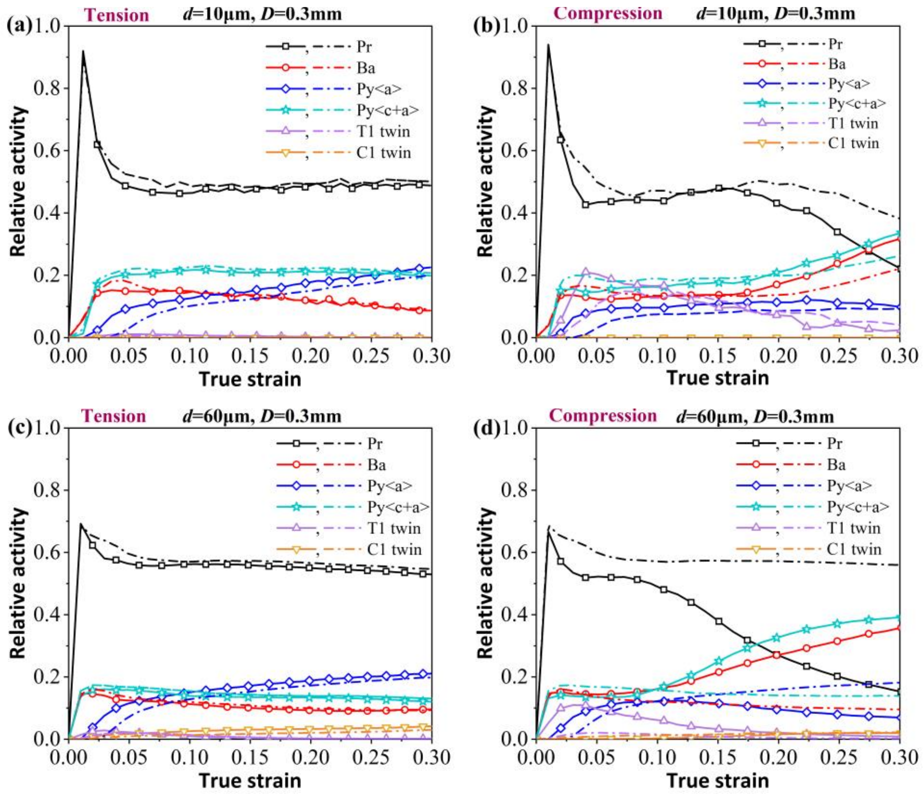

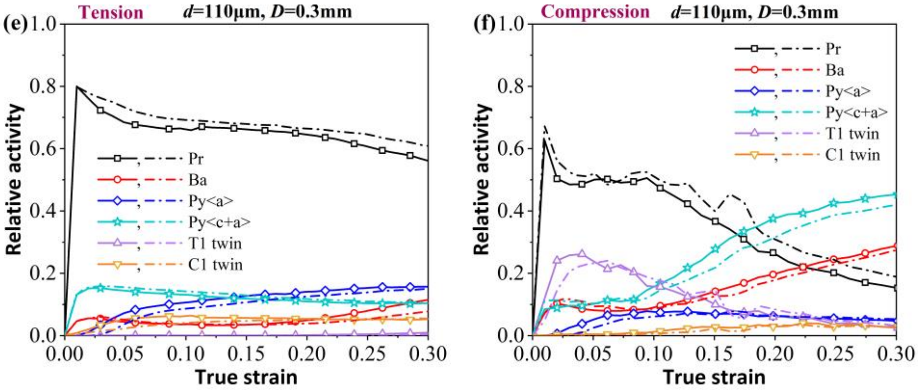

Fig. 7. Effect of grain size on the slip and twinning activity under tension/compression. (a) d=10μm, tension, (b) *d*=10μm, compression, (c) *d*=60μm, tension, (d) *d*=60μm, compression, (e) *d*=110μm, tension, and (f) *d*=110μm, compression. The dash dot line represents the simulated result without GND.

Effect of diameter on the average slip/twinning activity under tension/compression is shown in Fig. 8. In the tensile deformation, the C1 twin activity decreases with the diameter. The reduced twin activity then gives rise to the lower strain hardening rate of small diameter specimen, as shown in Fig 4c. This finding is consistent with the experimental result of (Zhu et al., 2022). They reported that the twin density decreases with the sample thickness in the tension of the ultra-thin CP-Ti sheet. However, the activity of T1 twin exhibits a contrary tendency in compression with the decrease of diameter (Fig. 8b,d,f), that is, the T1 twin is easier to be activated under small diameter in compression. More prevalent twin-dislocation interaction provided additional strain hardening and may result in high stress, resulting in the increased T-C asymmetry in small diameter specimen when $\varepsilon \geqslant 0.15$ (Fig. 5b). But in the meantime, the relative activity of pyramidal<c+a> and basal slip is decreased with diameter, which may lead to a lower strain hardening rate due to their high CRSS. This mechanism gains the upper hand since the simulated true stress is decreased with diameter in compression, as shown in Fig. 4d. While the experimental stress changes slightly with diameter in compression, which indicates the contribution from twin-dislocation interaction may be underestimated in the crystal plasticity model.

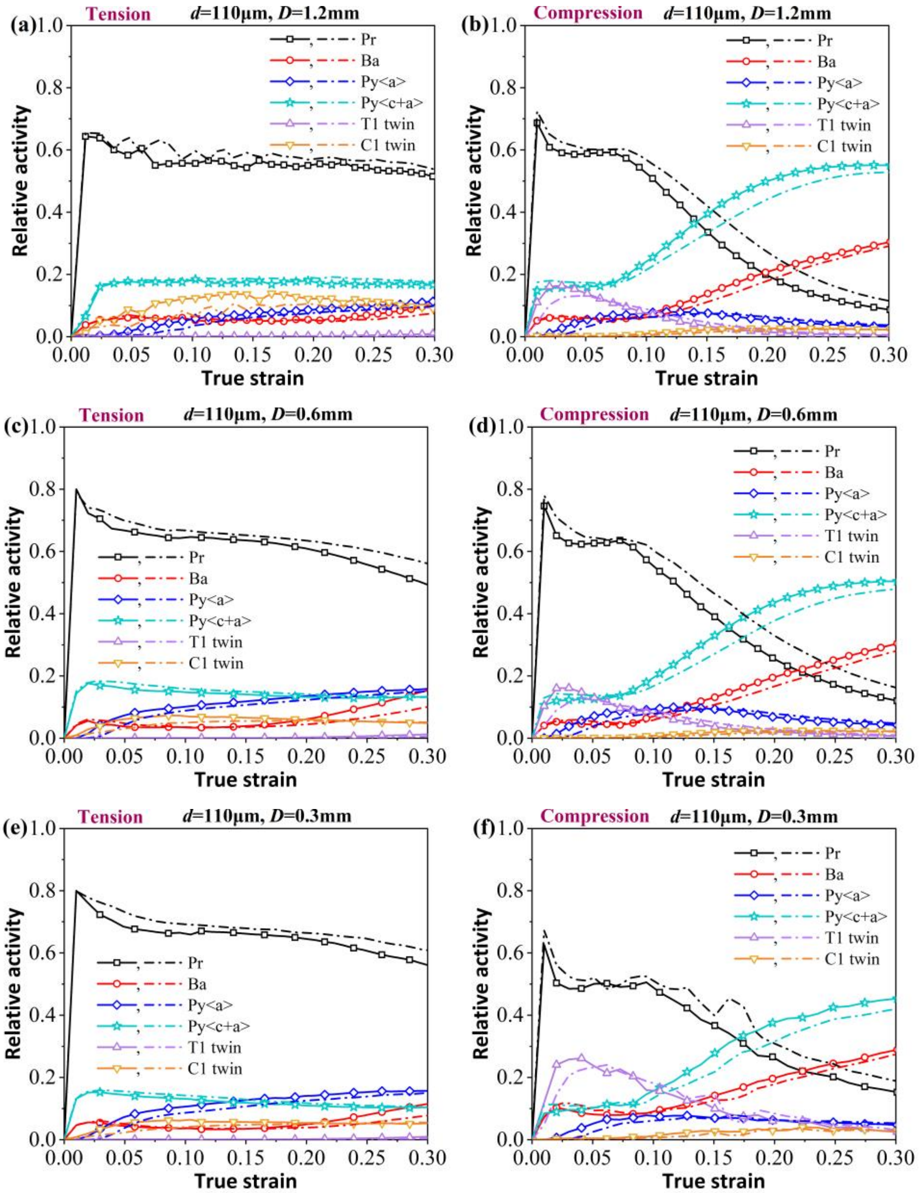

Fig. 8. Effect of diameter on the slip and twinning activity under tension (left column) and compression (right column). (a, b) *D*=1.2mm (c, d) *D*=0.6mm, and (e, f) *D*=0.3mm. The dash dot line represents the simulated result without GND.

4.3 Size-dependent fracture behavior

In meso/micro tension, the fracture strain generally decreases with increasing grain size and decreasing geometrical size (Fu and Chan, 2011; Li et al., 2019). High ductility is often reported in fine-grained materials (Fakhar and Sabbaghian, 2021; Gao et al., 2021). While in this study, some different results were obtained. The effect of diameter and grain size on the tensile stress, uniform strain, and fracture strain is illustrated in Fig. 9. The uniform and fracture strain are found to be smallest with *d*=10μm when *D* equals 1.2 and 0.6mm (Fig. 9b, d). The uniform and fracture strain slightly decreases when the grain size increases from 60 to 110μm. The abnormal high ductility in the coarse-grained sample is attributed to the high density twins as shown in Fig. 6. Deformation twins obstruct the dislocation motion and cause the dynamic Hall-Petch effect. It reorients grains into a hardening orientation and may stimulate the activation of hard slip mode that is difficult to activate in the original orientation. Both of these effects lead to the increased overall strain hardening (Fig. 9a, c, e) and enhance the ductility by delaying plastic instability (Barnett, 2007a; Jain et al., 2008). On the other hand, however, local stress concentration in the vicinity of TBs may trigger crack initiation and crack tends to propagate into region with high dislocation density (Jia et al., 2022). Especially the $\left\{10\bar{1}1\right\}-\left\{10\bar{1}2\right\}$ double twin constitutes potential site for crack initiation and may cause premature and catastrophic failure (Ando et al., 2014; Barnett, 2007b). The competition between these two opposite role of twins governs the grain size-dependent fracture behavior. The increased uniform and fracture strain in the coarse-grained sample in this study indicates that the positive effect of deformation twins on ductility gains the upper hand. The uniform and fracture strain decrease with diameter in various grain size samples. When the diameter reduces to 0.3mm, as shown in Fig. 9e, f, the ductility fine grain sample becomes the best. The uniform and fracture strain of coarse grain samples are dramatically decreased because severe strain localization may occur when the imposed strain is only accommodated by several grains. The grain scale strain pattern will analyzed in next section.

Fig.10 shows the SEM fractographs of tension samples with different grain sizes and diameters. The dashed line delineates the interface between fracture surface and free surface. It changes from a near-circular interface to a distorted one with the increasing grain size and decreasing diameter, indicating the homogenous deformation before failure. No obvious interface is observed in the fractography of sample with d=110μm and D=0.3μm. For the fine-grained samples, abundant equiaxed dimples can be found in the fracture surface regardless of the diameter, which manifests the typical ductile fracture mode. With the increase of grain size, the fraction of GB is reduced and thus resulting in less site for void nucleation (Li et al., 2019; Xu et al., 2015). From Fig. 8, fewer dimples are observed and the size of dimples is uneven in the fracture surface of samples with d=60, 110μm and D=1.2, 0.6mm. Some deep and large dimples are formed in these samples. This implies that the void could undergo a long period of growth and coalescence before evolving into a crack, resulting in the high uniform and fracture strain. This relationship between dimple size and ductility is consistent with the result of previous works (Das and Tarafder, 2008; Qin et al., 2019). When the diameter reduces to 0.3mm, deep dimples are rare for the samples with d=60μm, and some shallow dimples and elliptic facets are observed (Fig. 10f). For the samples with d=110μm, several prominent tearing ridges and some scattered voids can be found. The elliptic facet and tearing ridge indicate that the crack may propagate along a crystal or a GB, leading to reduced ductility (Fig. 9f).

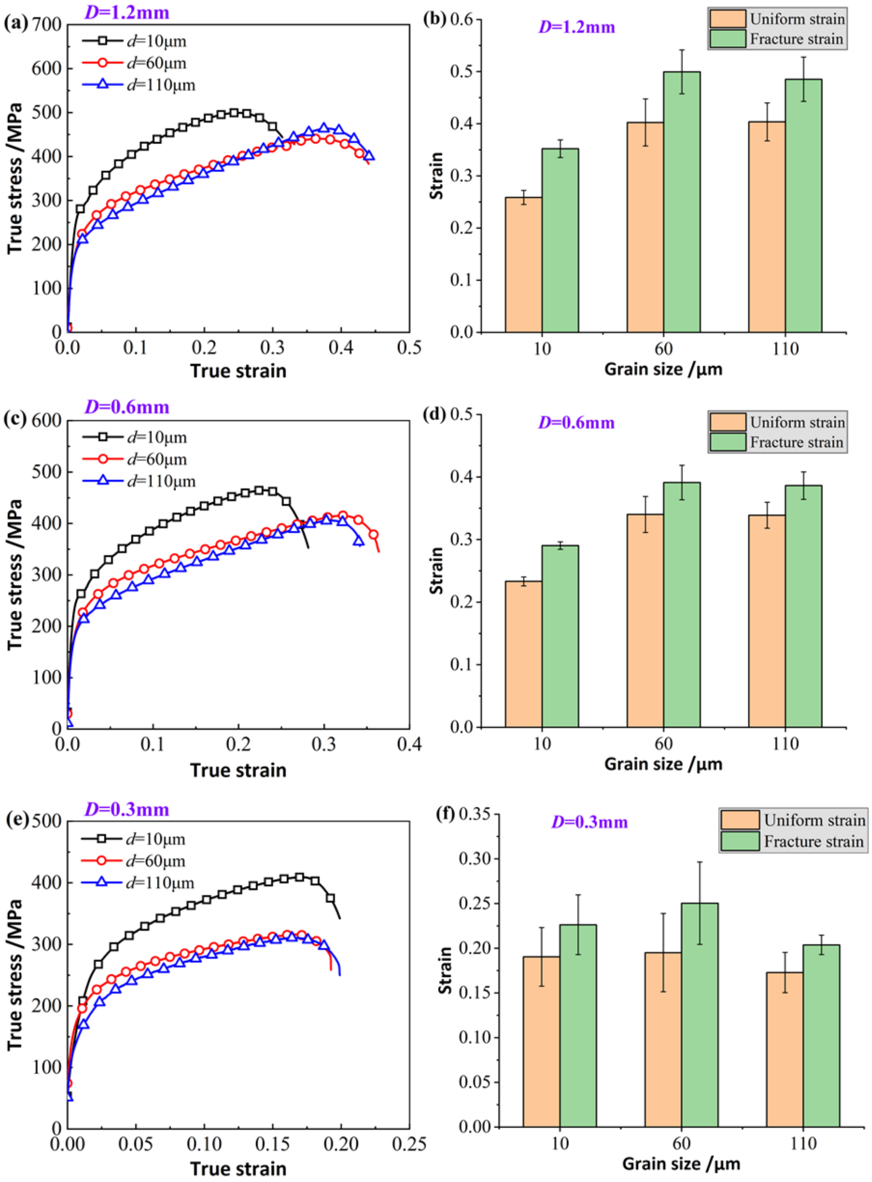

Fig. 9. Experimental tensile stress (left column) and uniform/fracture strain (right column) under diameters of 1.2mm (a, b), 0.6mm (c, d), and 0.3mm (e, f).

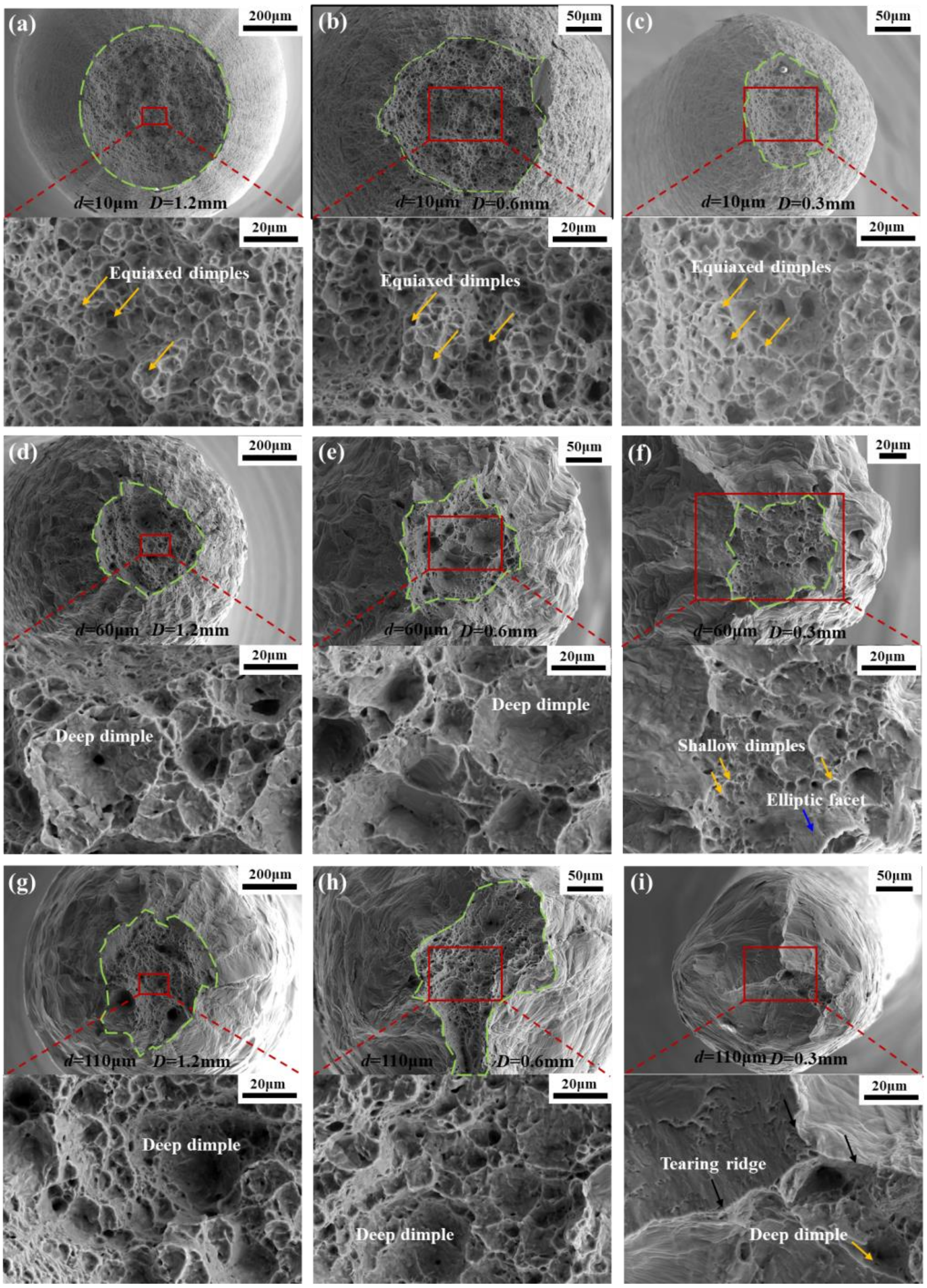

Fig. 10. SEM fractographs of tension samples with different grain sizes and diameters. (a-c) *d*=10μm, (d-f) *d*=60μm, and (g-i) *d*=110μm. Diameter equals to 1.2mm, 0.6mm, and 0.3mm, respectively, from left column to right column.

4.4 Grain scale strain and stress pattern

The effect of grain size and diameter on the strain pattern at grain scale after tension/compression to the global strain of 0.25 are shown in Fig. 11 and Fig. 12, respectively. In the fine-grained specimen, some evenly distributed strain hot spots and short shear bands are generated in tension and compression (Fig. 11a). While for the compressed sample, the strain value of the shear band is lower than the tension one. With the increase of grain size, the number of shear bands is decreased and the width and length of shear band is increased, indicating the strong strain inhomogeneous. A striking necking is observed in the tension of specimen with *d*=110μm since the slip or twinning may cluster in several grains when only few grains accommodate the imposed strain (Tang et al., 2019). This heterogeneous deformation is weakened with the increasing diameter. As demonstrated in Figs. 12a, b, some shear bands intertwine in the specimens with *D*=0.6 and 1.2mm. But the length and width of shear band are still larger than that of fine-grained specimen, which manifests that the width and length of local shear band are dependent on the grain size, i.e., larger grain size results in longer and wider shear band (Zhang et al., 2018).

Grain scale strain heterogeneity causes the roughening surface, which plays a critical role in damage initiation. Pronounced hills and valleys are observed in all the specimens, and the free surface becomes more roughen at coarse-grained specimens. The SEM observation in Fig. 10 verifies this result. It also coincides with the finding of (Wouters et al., 2005) that the surface roughness scales linearly with both strain and grain size. Comparing the tensile and compressed samples, it is found that the free surfaces are basically complementary to each other, i.e., a valley in tension becomes a hill in the compression counterpart and vice versa. For example, the valleys near grains A, B, C, and D in the tension become the hills at the same location.

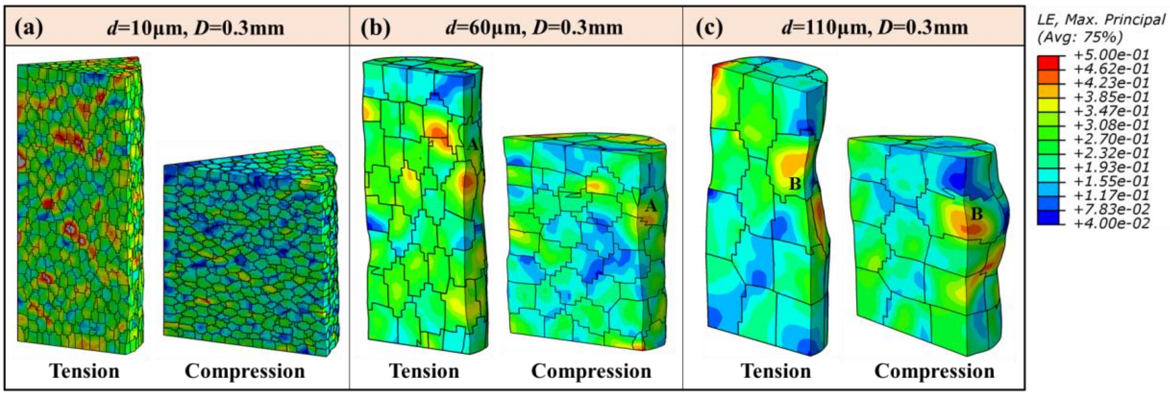

Fig. 11. Effect of grain size on the strain pattern after tension/compression to the global strain of 0.25. (a) *d*=10μm, *D*=0.3mm, (b) *d*=60μm, *D*=0.3mm, and (c) *d*=110μm, *D*=0.3mm.

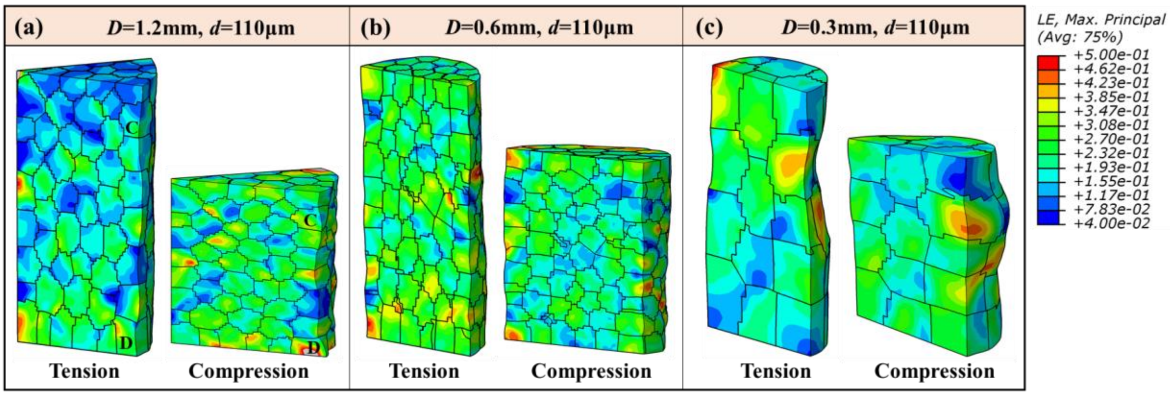

Fig. 12. Effect of diameter on the strain pattern after tension/compression to the global strain of 0.25. (a) *D*=1.2mm, *d*=110μm, (b) *D*=0.6mm, *d*=110μm, and (c) *D*=0.3mm, *d*=110μm.

The histograms of the relative frequency of logarithmic strain after tension/compression to 0.25 global strain are plotted in Fig. 13 to assess the strain heterogeneity and grain scale T-C asymmetry quantitatively. The frequency distributions of fine-grained sample and large diameter sample are well bell-shaped. The peak frequencies are high, indicating that the deformation is more uniform since very small and large strain frequencies are low. When the grain size increases from 10μm to 60μm, the frequency distribution in both tension and compression varies from the well bell-shaped to the irregular one (Fig. 13a). Peak frequencies are declined and the overall strain frequency becomes more widely spread, which means more severe strain heterogeneity. A diverse tendency is found in tension and compression when the grain size increases from 60μm to 110μm. The peak frequency gradually decreases with the increasing grain size in tension and large strain (>0.4) appears with a certain frequency. While the peak frequency inversely rises from 0.056 to 0.061 when the grain size increases from 60μm to 110μm. It is attributed to the plentiful twinning activity in the compression of coarse-grained sample. Deformation twinning accommodates strain along *c*-axis via a stepwise sequential process from creating an embryo to the propagation of a twin embryo into a twin lamella (Kumar and Beyerlein, 2020; Kumar et al., 2018). On the other hand, twinning induced reorientation gives arise to the activation of non-prismatic slip that accommodates strain along various directions as shown in Fig. 7, results in more homogeneous deformation. In regard of the diameter effect, this twinning induced strain homogenization is also effective. When the diameter is reduced from 0.6mm to 0.3mm, the strain frequency shows a right-skewed platykurtic distribution in the tension scenario, whereas the distribution curves are very close in compression due to the enhanced twinning activity, as shown in Fig. 8f.

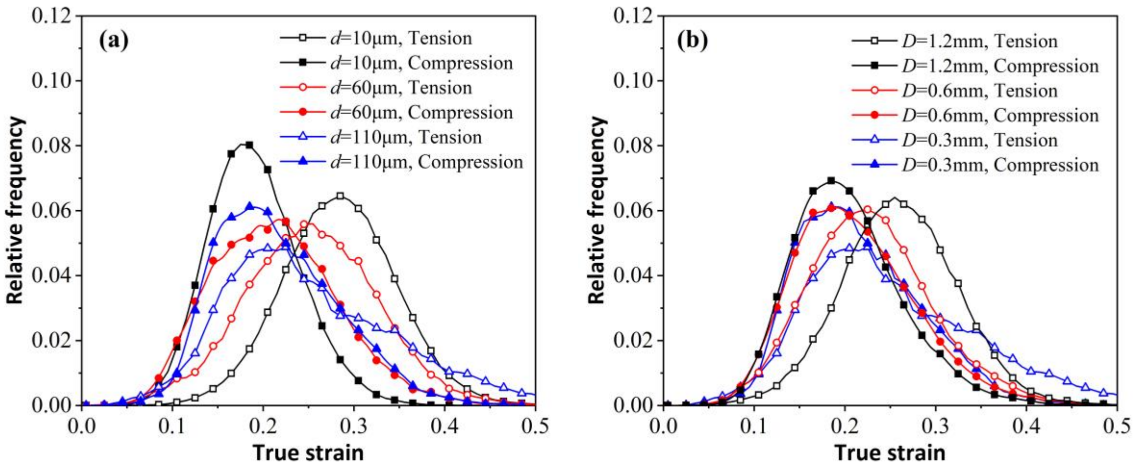

Fig. 13. Relative frequency of logarithmic strain after tension/compression to the global strain of 0.25. (a) effect of grain size and (b) effect of diameter.

The effect of grain size on the distribution of mises stress after tension/compression to the global strain of 0.25 is shown in Fig 14. In line with the macro mechanical response, the mises stress in compression is generally higher than the tension one due to the more prevailing twins and activation of slip mode with high CRSS. The stress near GBs is higher than that in grain interiors because the orientation mismatch of neighboring grains creates high density of GND and SSD (Fig. 18). Especially at the triple GB junction, some stress hot spots can be found. The stress concentrating at GBs could trigger the initiation of micro-crack. As the grain size increases, the number of stress hot spots at GBs is reduced. The potential site for initiation of micro-void is then decreased, resulting in the fewer dimples as shown in Fig. 10. From the stress distribution of samples with *d*=60 and 110μm, it is intuitively observed that the stress at grains that occupy free surface is lower than that of interior grains. To quantitatively evaluate the free surface effect, the average stress varying from left to right margin along the radial direction in a longitudinal section is plotted in Fig. 15. Note that the abscissa is the distance from the left margin or axis of symmetry of the sample before deformation. The stress is obviously reduced near the sample margin. The reduction widths of the sample with *d*=10, 60, and 110μm are 12, 72, and 96μm, respectively, which are very close to the average grain size. It indicates that the free surface layer is quite soft and the influence domain is about one grain.

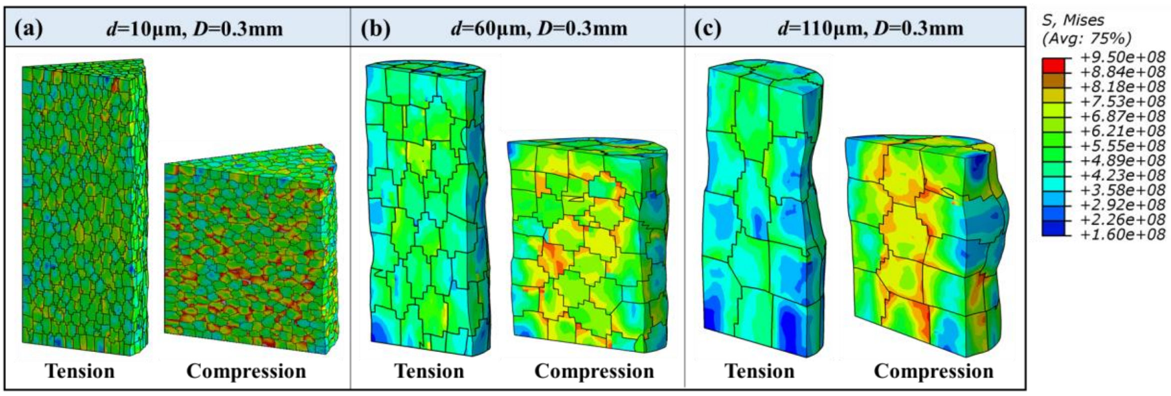

Fig. 14. Effect of grain size on the mises stress pattern after tension/compression to the global strain of 0.25. (a) *d*=10µm, *D*=0.3mm, (b) *d*=60µm, *D*=0.3mm, and (c) *d*=110µm, *D*=0.3mm.

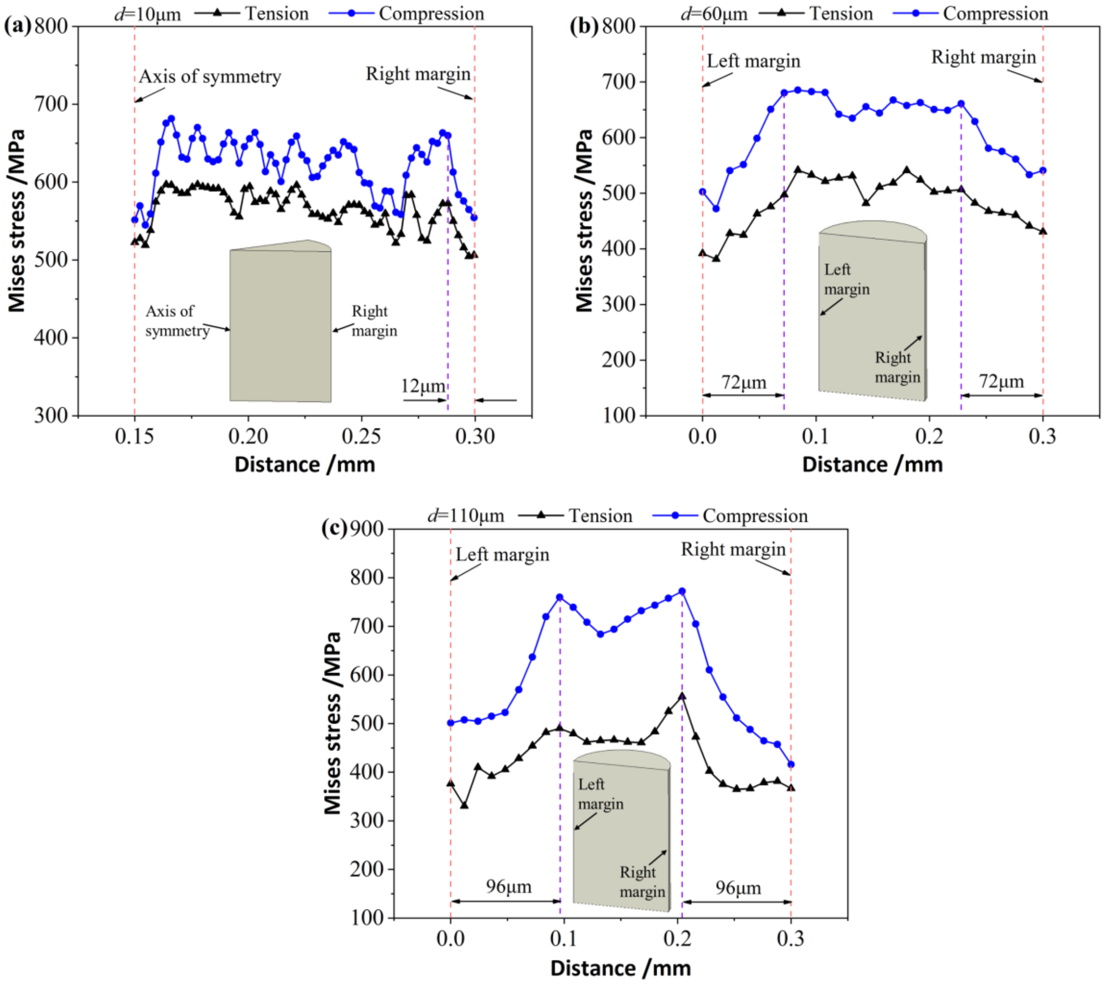

Fig. 15. Average stress of samples with different grain sizes varying from left to right margin along the radial direction. (a) *d*=10µm, (b) *d*=60µm, and (c) *d*=110µm.

Fig. 16 shows the effect of diameter on the distribution of mises stress after tension/compression to the global strain of 0.25. The stress at interior grains is increased with the decreasing diameter due to the higher twin activity and SSD density in this region of small sample (Fig. 20). The average stress samples with different diameters varying from left to right margin along the radial direction in a longitudinal section also exhibits an apparent reduction in stress near the margin (Fig. 17). The average width of the softening area of sample with *d*=110μm and various diameters is 104.3μm, which further demonstrates that the influence domain of softening free surface is about one grain layer.

The surface layer model, mixed constitutive model, and grain boundary strengthening model are the frequently-used phenomenon constitutive models describing the size-dependent mechanical response (Lai et al., 2008; Li et al., 2019; Yun et al., 2010). In these models, the specimen is usually assumed to consist of three portions with different strengths, viz., surface grains, grain interior, and GBs. The flow stress σ could be expressed as:

$$\sigma = f_{\mathrm{surf}}\sigma_{\mathrm{surf}} + f_{\mathrm{gb}}\sigma_{\mathrm{gb}} + f_{\mathrm{gi}}\sigma_{\mathrm{gi}} \quad \text{with} \quad f_{\mathrm{surf}} + f_{\mathrm{gb}} + f_{\mathrm{gi}} = 1 \tag{36}$$

where σ_{surf}, and f_{surf} are the stress and fraction of surface grains, σ_{gb} and f_{gb} are the stress and fraction of GBs , σ_{gi} and f_{gi} are the stress and fraction of grain interior. The GBs is harder than the grain interior and the surface grain is weaker than the internal portion because the resistance to dislocation motion at surface grain is low and it is easy to rotate to accommodate the strain incompatibility due to few constraints. From Figs. 15 and 17, the full-field simulation successfully captures the softening effect of surface grains in a natural way, and the strengthening of GBs is described by GND. Although the stress at interior grains is higher in the small specimen, the fraction of surface grains is also increased and the softening effect of surface grains is dominant, resulting in the reduced global stress, as shown in Fig. 4.

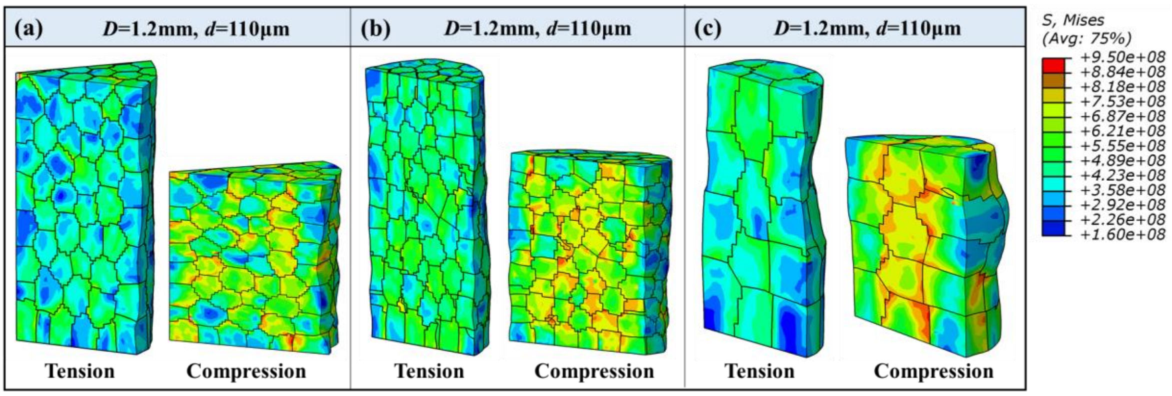

Fig. 16. Effect of diameter on the stress pattern after tension/compression to the global strain of 0.25. (a) *D*=1.2mm, *d*=110μm, (b) *D*=0.6mm, *d*=110μm, and (c) *D*=0.3mm, *d*=110μm.

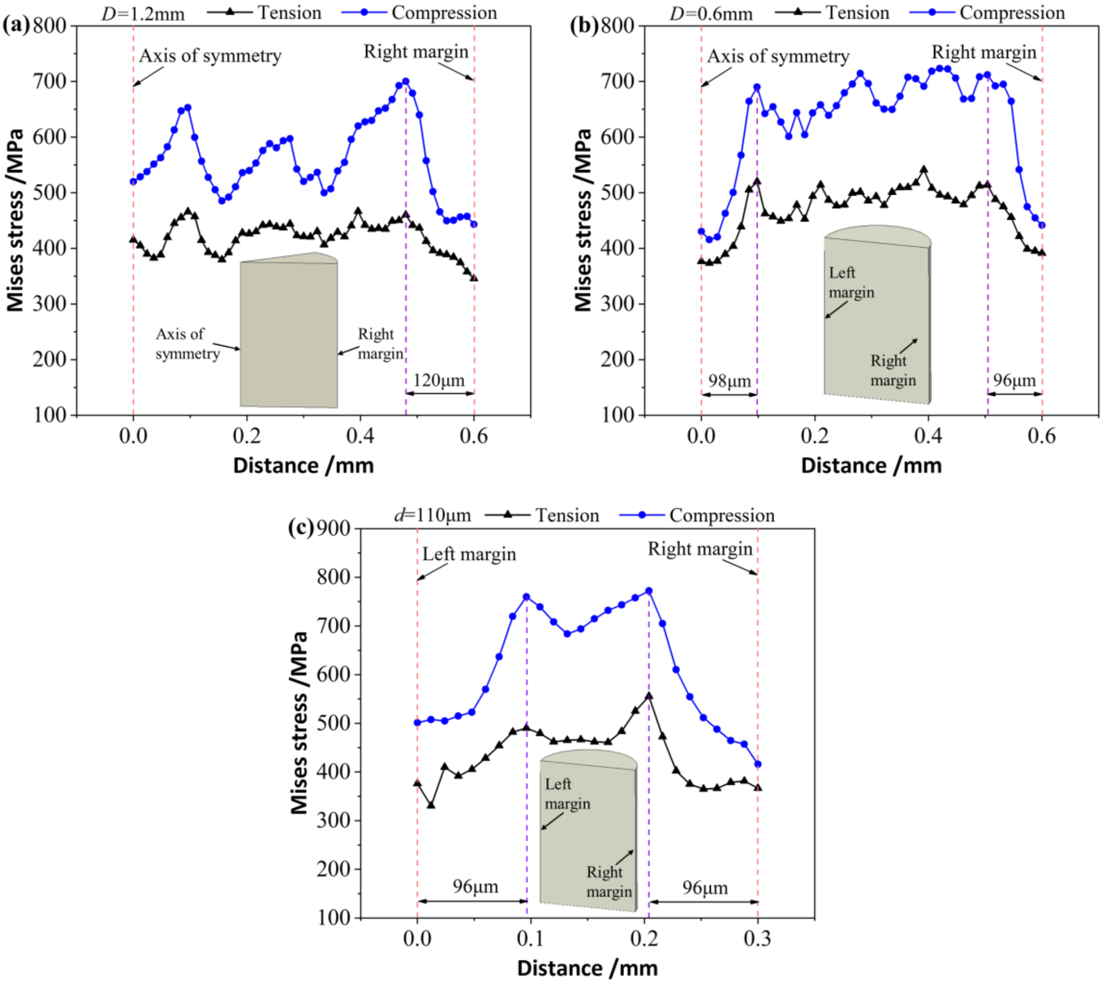

Fig. 17. Average mises stress of samples with different diameters varying from left to right margin along the radial direction. (a) *D*=1.2mm, (b) *D*=0.6mm, and (c) *D*=0.3mm.

4.5 Dislocation density

Fig. 18 shows the effect of grain size on the density distribution of total SSD and GND after tension/compression to a global strain of 0.25. GND mainly accumulates in the vicinity of GBs due to the high strain gradient caused by the misorientation of adjacent grains. The SSD density has relatively uniform distribution within the grains. Some hot spots of SSD density are observed near GBs, especially at the triple GB junction, similar to the mises stress distribution (Fig. 14). The high density of GND at GBs arrests more SSD and thus causes stress concentration. A general decreasing trend of SSD density can be found with the increase of grain size. The GND density is also higher in fine-grained samples, which provides higher resistance to dislocation slip and enhances the strength of material. The correlation between grain size and average GND density is shown in Fig. 19. A strong linear relation is found between $\sqrt{\rho_{\mathrm{GND}}}$ and $1/\sqrt{d}$. Considering the Taylor equation for dislocation strengthening

($\sigma = \alpha\mu b\sqrt{\rho}$) (Taylor, 1934), it implies that the strengthen contributed by GND follows the typical Hall-Petch relationship that commonly used to charactering the grain size effect. The slope increases a little with strain, indicating the high grain size dependence at large strain. In addition, the average GND density under tension is higher than that of compression, especially at large strain, which means that the strain heterogeneity is more severe under tension.

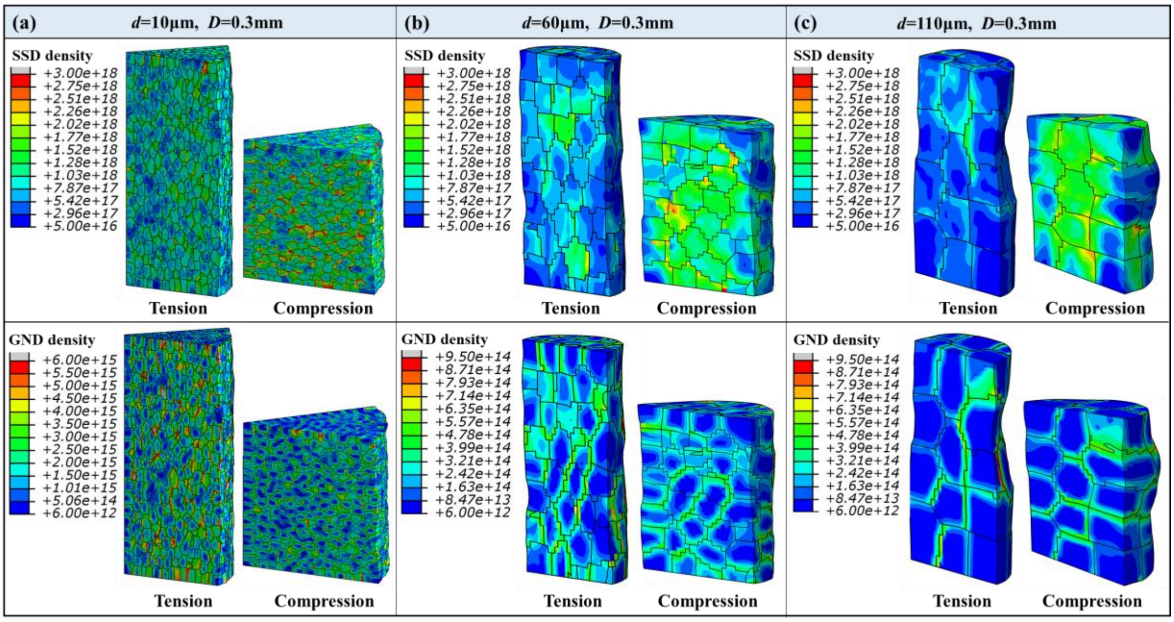

Fig. 18. Effect of grain size on the total density distribution of SSD and GND after tension/compression to a global strain of 0.25. (a) *d*=10μm, *D*=0.3mm, (b) *d*=60μm, *D*=0.3mm, and (c) *d*=110μm, *D*=0.3mm.

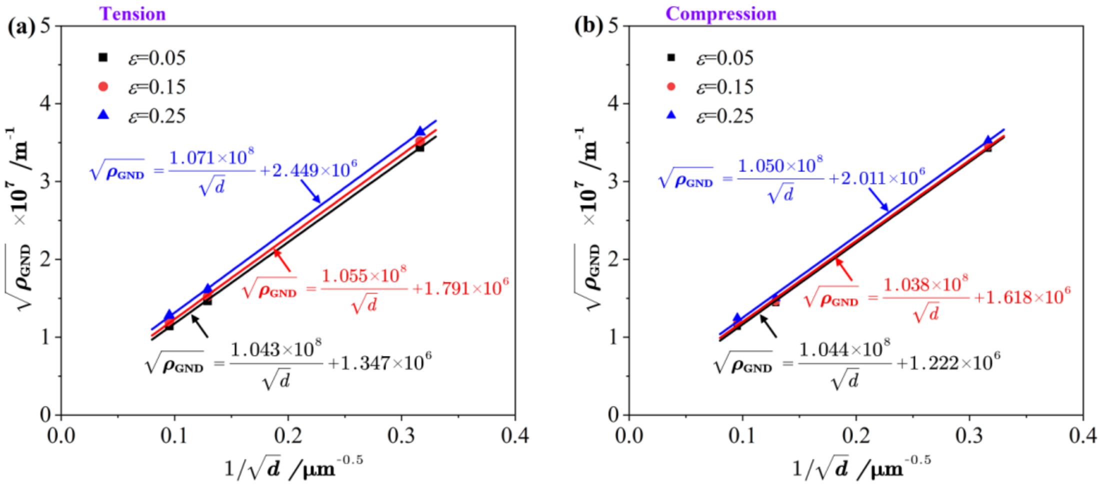

Fig. 19. Correlation between grain size and average density of GND under (a) tension and (b) compression.

The effect of diameter on the total density distribution of SSD and GND after tension/compression to a global strain of 0.25 is illustrated in Fig. 20. The SSD density at surface grains is generally lower than inner grains. From the average SSD density varying from left to right margin along radial direction (Fig. 21), it shows a clear reduction in SSD density near the free surface. The width of low SSD density area is the same as the low stress region (Fig. 17). The distribution of SSD and GND support the interpretation of the surface layer model, mixed constitutive model, and grain boundary strengthening model. That is, the dislocation is easier to pile up at GBs than grain interior and the resistance to dislocation motion at surface grain is low.

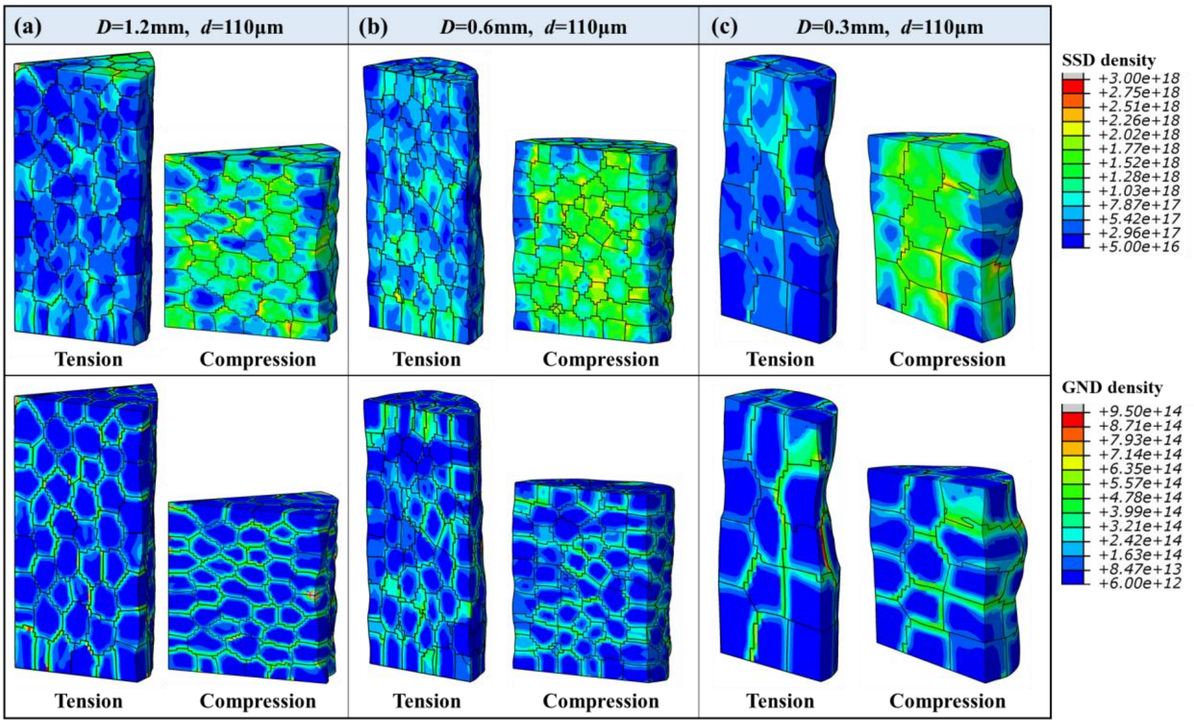

Fig. 20. Effect of diameter on the total density distribution of SSD and GND after tension/compression to a global strain of 0.25. (a) *D*=1.2mm, *d*=110μm, (b) *D*=0.6mm, *d*=110μm, and (c) *D*=0.3mm, *d*=110μm.

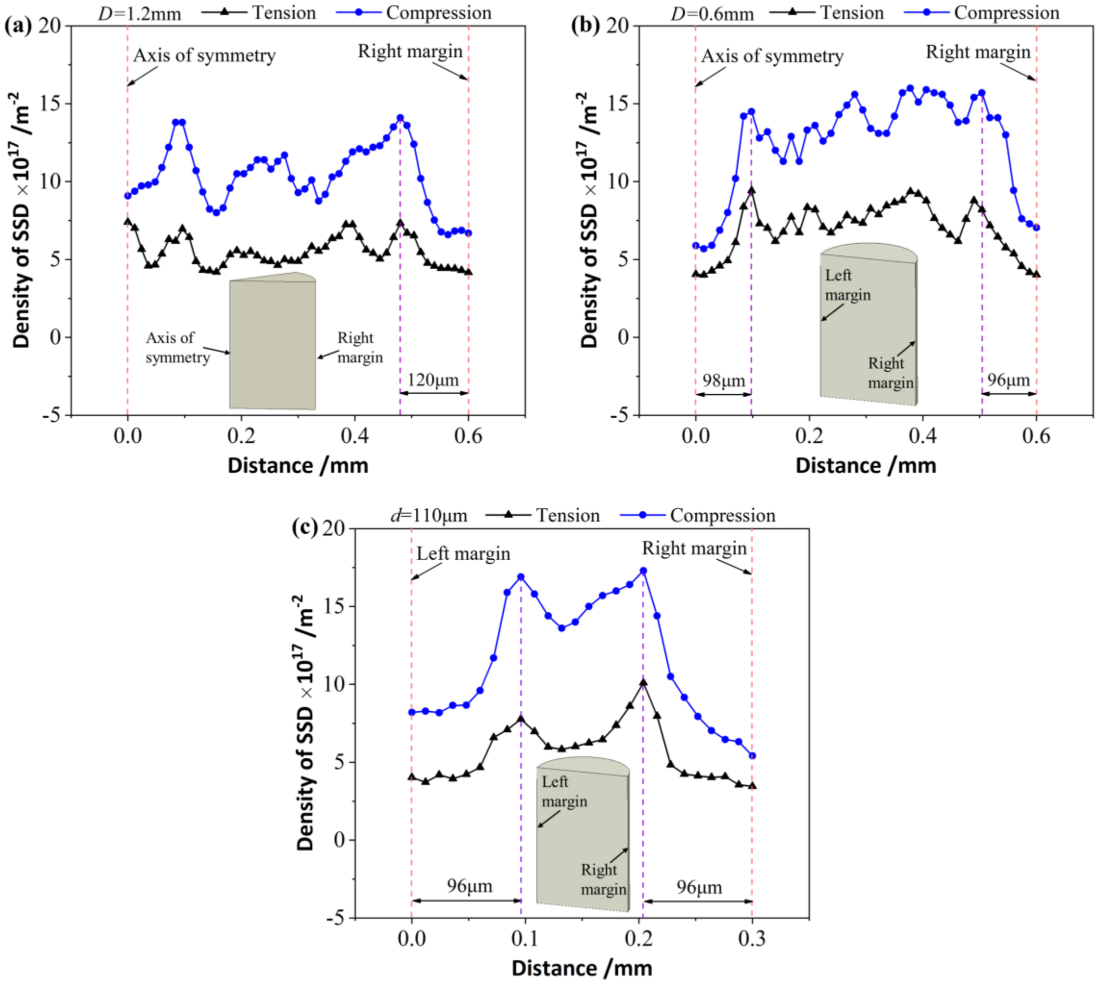

Fig. 21. Average SSD density of samples with different diameters varying from left to right margin along radial direction. (a) *D*=1.2mm, (b) *D*=0.6mm, and (c) *D*=0.3mm.

5. Conclusions

In this research, a mechanism-based non-local crystal plasticity model was established . It successfully predicted the size-dependent mechanical response in both the tension and compression of CP-Ti. The size-dependent T-C asymmetric yielding and strain hardening was well captured by the non-local model. Without considering GND, the grain size effect was weakenly represented and it was found that the twin activity was slow down and the relative activities of pyramidal<c+a> and basal slip were decreased. Coupling micro-tension/compression test and full-field simulation, the synergistic effects of dislocation slip, deformation twining, and GBs on size-dependent fracture behavior, plastic heterogeneity and T-C asymmetry during micro-scaled deformation of CP-Ti were unraveled. Primary conclusions were drawn as:

(1) Deformation twinning is easier to activation in compression, it reorients the crystal and

induces the activation of pyramidal<c+a> and basal slip, leading to the secondary hardening due to their higher CRSS and more severe T-C asymmetry in flow increases at larger strain. T-C asymmetry in flow stress is enhanced with the increasing grain size and the decreasing dimeter of specimen. The difference in the activity of pyramidal<c+a> and basal slip, and T1 twin between tension and compression is increased with grain size, which is responsible for the enhanced T-C asymmetry in coarse-grained specimen.

(2) In the sample with $D \geqslant 0.6$mm, the ductility of CP-Ti is enhanced with grain size due to the more prevailing twins. Twinning induced reorientation activates the hard slip mode such as pyramidal<c+a> and basal slip. The concentrated stress could be relieved by such abundant slip rather than cracking, resulting in high ductility. Less but larger and deeper dimples were generated at the fracture surface of coarse-grained samples with $D \geqslant 0.6$ mm. The void could undergo a long period of growth and coalescence before evolving into a crack. The uniform and fracture strain of coarse grain samples are dramatically decreased when diameter decreases to 0.3 mm and several elliptic facet and large tearing ridge, indicating the transition of fracture mode from ductile fracture to brittle fracture when the imposed strain is only accommodated by a few grains.

(3) Grain scale strain heterogeneity also shows a T-C asymmetry, viz., grain scale deformation is more inhomogeneous in tension. From statistical perspective, the deformation is more homogeneous in compression when d is increased from 60 to 110 μm. It is attributed to the plentiful twinning activity in the compression of coarse grain samples since more activation of non-prismatic slips accommodates strain along various directions.

(4) GNDs are accumulated in the vicinity of GBs and blocks more SSDs, resulting in the higher stress near GBs than grain interior. The strengthen contributed from GND follows the Hall-Petch law. The average GND density under tension is higher than that of compression, especially at large strain, it also demonstrates the severer strain heterogeneity under tension. The SSD density at surface grains is generally lower than that in inner grains, leading to the soft layer near free surface. The width of soft layer is about one grain.

Acknowledgments

The authors would like to acknowledge the funding support to this research from the National Natural Science Foundation of China (No. 52090043, No. 52105337, No. 51835011), the projects of 1-ZE1W and BBAT from The Hong Kong Polytechnic University, and the project of No. 15223520 from the General Research Fund.

CRediT authorship contribution statement

Xuefeng Tang: Conceptualization, Methodology, Software, Data curation, Writing – original draft; Zhizhou Wang: Experiments, Visualization, Writing – review & editing; Lei Deng: Experiments, Formal analysis, Validation, Writing – review & editing; Mao Zhang: Formal analysis, Validation, Writing – review & editing; Pan Gong: Data curation, Visualization, Writing – review & editing; Junsong Jin: Formal analysis, Data curation, Writing – review & editing; Xinyun Wang: Project administration, Funding acquisition, Resources, Writing - Review & Editing; M.W. Fu: Conceptualization, Funding acquisition, Writing - Review & Editing.

Declaration of Competing Interest

The authors declare that they have no known competing financial interests or personal relationships that could have appeared to influence the work reported in this paper.

References

Abdolvand, H., Wright, J., Wilkinson, A.J., 2018. Strong grain neighbour effects in polycrystals. Nat Commun 9, 171.

Acharya, A., Bassani, J.L., 2000. Lattice incompatibility and a gradient theory. Journal of the Mechanics and Physics of Solids 48, 1565-1596.

Ando, D., Koike, J., Sutou, Y., 2014. The role of deformation twinning in the fracture behavior and mechanism of basal textured magnesium alloys. Materials Science and Engineering: A 600, 145-152.

Arentoft, M., Eriksen, R.S., H.N.Hansen, Paldan, N.A., 2011. Towards the first generation micro bulk forming system. CIRP Annals 60, 335-338.

ARSENLIS, A., PARKS, D.M., 1999. CRYSTALLOGRAPHIC ASPECTS OF GEOMETRICALLY-NECESSARY AND STATISTICALLY-STOREDDISLOCATION DENSITY. Acta Materialia 47, 1597-1611.

Asaro, R.J., Rice, J.R., 1977. Strain localization in ductile single crystals. Journal of the Mechanics and Physics of Solids 25, 309-338.

Banerjee, D., Williams, J.C., 2013. Perspectives on Titanium Science and Technology. Acta Materialia 61, 844-879.

Baral, M., Hama, T., Knudsen, E., Korkolis, Y.P., 2018. Plastic deformation of commercially-pure titanium: experiments and modeling. International Journal of Plasticity 105, 164-194.

Barnett, M.R., 2007a. Twinning and the ductility of magnesium alloys: Part I:“Tension” twins. Materials Science and Engineering: A 464, 1-7.

Barnett, M.R., 2007b. Twinning and the ductility of magnesium alloys: Part II.“Contraction” twins. Materials Science and Engineering: A 464, 8-16.

Baudoin, P., Hama, T., Takuda, H., 2019. Influence of critical resolved shear stress ratios on the response of a commercially pure titanium oligocrystal: crystal plasticity simulations and experiment. International Journal of Plasticity 115, 111-131.

Belyschko, T., Krongauz, Y., Organ, D., Fleming, M., Krysl, P., 1996. Meshless methods: An overview and recent developments. Computer Methods in Applied Mechanics and Engineering 139, 3-47.

Britton, T.B., Dunne, F.P.E., Wilkinson, A.J., 2015. On the mechanistic basis of deformation at the microscale in hexagonal close-packed metals. Proceedings of the Royal Society A: Mathematical, Physical and Engineering Sciences 471.

Busso, E.P., Meissonnier, F.T., O'Dowd, N.P., 2000. Gradient-dependent deformation of two-phase single crystals. Journal of the Mechanics and Physics of Solids 48, 2333-2361.

Cepeda-Jiménez, C.M., Molina-Aldareguia, J.M., Pérez-Prado, M.T., 2015. Origin of the twinning to slip transition with grain size refinement, with decreasing strain rate and with increasing temperature in magnesium. Acta Materialia 88, 232-244.

Cermelli, P., Gurtin, M.E., 2001. On the characterization of geometrically necessary dislocations in finite plasticity. Journal of the Mechanics and Physics of Solids 49, 1539-1568.

Cheng, J., Shen, J., Mishra, R.K., Ghosh, S., 2018. Discrete twin evolution in Mg alloys using a novel crystal plasticity finite element model. Acta Materialia 149, 142-153.

Cheong, K.S., Busso, E.P., Arsenlis, A., 2005. A study of microstructural length scale effects on the behaviour of FCC polycrystals using strain gradient concepts. International Journal of Plasticity 21, 1797-1814.

Christian, J.W., Mahajan, S., 1995. DEFORMATION TWINNING. Progress in Materials Science 39, 1-157.

Clausen, B., Tomé, C.N., Brown, D.W., Agnew, S.R., 2008. Reorientation and stress relaxation due to twinning: Modeling and experimental characterization for Mg. Acta Materialia 56, 2456-2468.

Counts, W.A., Braginsky, M.V., Battaile, C.C., Holm, E.A., 2008. Predicting the Hall–Petch effect in fcc metals using non-local crystal plasticity. International Journal of Plasticity 24, 1243-1263.

Das, A., Tarafder, S., 2008. Geometry of dimples and its correlation with mechanical properties in austenitic stainless steel. Scripta Materialia 59, 1014-1017.

Demir, E., Gutierrez-Urrutia, I., 2021. Investigation of strain hardening near grain boundaries of an aluminum oligocrystal: Experiments and crystal based finite element method. International Journal of Plasticity 136.

Dunne, F.P.E., Kiwanuka, R., Wilkinson, A.J., 2012. Crystal plasticity analysis of micro-deformation, lattice rotation and geometrically necessary dislocation density. Proceedings of the Royal Society A: Mathematical, Physical and Engineering Sciences 468, 2509-2531.

Dunne, F.P.E., Rugg, D., Walker, A., 2007. Lengthscale-dependent, elastically anisotropic, physically-based hcp crystal plasticity: Application to cold-dwell fatigue in Ti alloys. International Journal of Plasticity 23, 1061-1083.

Efstathiou, C., Sehitoglu, H., Lambros, J., 2010. Multiscale strain measurements of plastically deforming polycrystalline titanium: Role of deformation heterogeneities. International Journal of Plasticity 26, 93-106.

Evers, L., 2004. Non-local crystal plasticity model with intrinsic SSD and GND effects. Journal of the Mechanics and Physics of Solids 52, 2379-2401.

Fakhar, N., Sabbaghian, M., 2021. A good combination of ductility, strength, and corrosion resistance of fine-grained ZK60 magnesium alloy produced by repeated upsetting process for biodegradable applications. Journal of Alloys and Compounds 862.

Flipon, B., Keller, C., Quey, R., Barbe, F., 2020. A full-field crystal-plasticity analysis of bimodal polycrystals. International Journal of Solids and Structures 184, 178-192.

Fu, M.W., Chan, W.L., 2011. Geometry and grain size effects on the fracture behavior of sheet metal in micro-scale plastic deformation. Materials & Design 32, 4738-4746.

Fu, M.W., Wang, J.L., 2021. Size effects in multi-scale materials processing and manufacturing. International Journal of Machine Tools and Manufacture 167.

Fu, M.W., Wang, J.L., Korsunsky, A.M., 2016. A review of geometrical and microstructural size effects in micro-scale deformation processing of metallic alloy components. International Journal of Machine Tools and Manufacture 109, 94-125.

Gao, J., Jiang, S., Zhang, H., Huang, Y., Guan, D., Xu, Y., Guan, S., Bendersky, L.A., Davydov, A.V., Wu, Y., Zhu, H., Wang, Y., Lu, Z., Rainforth, W.M., 2021. Facile route to bulk ultrafine-grain steels for high strength and ductility. Nature 590, 262-267.

Githens, A., Ganesan, S., Chen, Z., Allison, J., Sundararaghavan, V., Daly, S., 2020. Characterizing microscale deformation mechanisms and macroscopic tensile properties of a high strength magnesium rare-earth alloy: A combined experimental and crystal plasticity approach. Acta Materialia 186, 77-94.

Guo, B., Gong, F., Wang, C., Shan, D., 2010. Size effect on friction in scaled down strip drawing. Journal of Materials Science 45, 4067-4072.

Guo, N., Wang, J., Sun, C.Y., Zhang, Y.F., Fu, M.W., 2020. Analysis of size dependent earing evolution in micro deep drawing of TWIP steel by using crystal plasticity modeling. International Journal of Mechanical Sciences 165.

Gurtin, M.E., 2002. A gradient theory of single-crystal viscoplasticity that accounts for geometrically necessary dislocations. Journal of the Mechanics and Physics of Solids 50, 5-32.

Habib, S.A., Khan, A.S., Gnäupel-Herold, T., Lloyd, J.T., Schoenfeld, S.E., 2017. Anisotropy, tension-compression asymmetry and texture evolution of a rare-earth-containing magnesium alloy sheet, ZEK100, at different strain rates and temperatures: Experiments and modeling. International Journal of Plasticity 95, 163-190.

Hama, T., Kobuki, A., Takuda, H., 2017. Crystal-plasticity finite-element analysis of anisotropic deformation behavior in a commercially pure titanium Grade 1 sheet. International Journal of Plasticity 91, 77-108.

Hama, T., Nagao, H., Kobuki, A., Fujimoto, H., Takuda, H., 2015. Work-hardening and twinning behaviors in a commercially pure titanium sheet under various loading paths. Materials Science and Engineering: A 620, 390-398.

Haouala, S., Lucarini, S., Llorca, J., Segurado, J., 2020. Simulation of the Hall-Petch effect in FCC polycrystals by means of strain gradient crystal plasticity and FFT homogenization. Journal of the Mechanics and Physics of Solids 134.

Hartl, C., 2019. Review on Advances in Metal Micro-Tube Forming. Metals 9.

Hestroffer, J.M., Latypov, M.I., Stinville, J.-C., Charpagne, M.-A., Valle, V., Miller, M.P., Pollock, T.M., Beyerlein, I.J., 2022. Development of grain-scale slip activity and lattice rotation fields in Inconel 718. Acta Materialia 226.

Hielscher, R., Schaeben, H., 2008. A novel pole figure inversion method: specification of theMTEXalgorithm. Journal of Applied Crystallography 41, 1024-1037.

Hosford, W.F., 1993. The mechanics of crystals and textured polycrystals. Oxford University Press.

Houtte, P.V., 1978. Simulation of the rolling and shear texture of brass by the Taylor theory adapted for mechanical twinning. Acta Metallurgica 26, 591-604.

Jain, A., Duygulu, O., Brown, D.W., Tomé, C.N., Agnew, S.R., 2008. Grain size effects on the tensile properties and deformation mechanisms of a magnesium alloy, AZ31B, sheet. Materials Science and Engineering: A 486, 545-555.

Jia, Y., Jiang, S., Tan, J., Lu, Z., Jiang, J., Wang, X., 2022. The evolution of local stress during deformation twinning in a Mg-Gd-Y-Zn alloy. Acta Materialia 222.

Kalidindi, S.R., 1998. Incorporation of deformation twinning in rystal plasticity models. Journal of the Mechanics and Physics of Solids 46, 267-290.

Kaur, M., Singh, K., 2019. Review on titanium and titanium based alloys as biomaterials for orthopaedic applications. Mater Sci Eng C Mater Biol Appl 102, 844-862.

Kim, H., Barlat, F., Lee, Y., Zaman, S.B., Lee, C.S., Jeong, Y., 2018. A crystal plasticity model for describing the anisotropic hardening behavior of steel sheets during strain-path changes. International Journal of Plasticity 111, 85-106.

Kim, J.-Y., Jang, D., Greer, J.R., 2012. Crystallographic orientation and size dependence of tension–compression asymmetry in molybdenum nano-pillars. International Journal of Plasticity 28, 46-52.

Knezevic, M., Lebensohn, R.A., Cazacu, O., Revil-Baudard, B., Proust, G., Vogel, S.C., Nixon, M.E., 2013.

Modeling bending of α-titanium with embedded polycrystal plasticity in implicit finite elements. Materials Science and Engineering: A 564, 116-126.

Kocks, U.F., Argon, A.S., Ashby, M.F., 1975. Thermodynamics and kinetics of slip. Progress in Materials Science 19, 1-281.

Kumar, M.A., Beyerlein, I.J., 2020. Local microstructure and micromechanical stress evolution during deformation twinning in hexagonal polycrystals. Journal of Materials Research 35, 217-241.

Kumar, M.A., Wroński, M., McCabe, R.J., Capolungo, L., Wierzbanowski, K., Tomé, C.N., 2018. Role of microstructure on twin nucleation and growth in HCP titanium: A statistical study. Acta Materialia 148, 123-132.

Kurukuri, S., Worswick, M.J., Ghaffari Tari, D., Mishra, R.K., Carter, J.T., 2014. Rate sensitivity and tension-compression asymmetry in AZ31B magnesium alloy sheet. Philos Trans A Math Phys Eng Sci 372, 20130216.

Lai, X., Peng, L., Hu, P., Lan, S., Ni, J., 2008. Material behavior modelling in micro/meso-scale forming process with considering size/scale effects. Computational Materials Science 43, 1003-1009.

Levy, M., Bass, H.E., Stem, R.R., 2001. Handbook of Elastic Properties of Solids, Liquids, and Gases. Academic Press.

Li, W.T., Li, H., Fu, M.W., 2019. Interactive effect of stress state and grain size on fracture behaviours of copper in micro-scaled plastic deformation. International Journal of Plasticity 114, 126-143.

Lim, H., Carroll, J.D., Battaile, C.C., Buchheit, T.E., Boyce, B.L., Weinberger, C.R., 2014. Grain-scale experimental validation of crystal plasticity finite element simulations of tantalum oligocrystals. International Journal of Plasticity 60, 1-18.

Lin, P., Hao, Y., Zhang, B., Zhang, S., Chi, C., Shen, J., 2017. Tension-compression asymmetry in yielding and strain hardening behavior of CP-Ti at room temperature. Materials Science and Engineering: A 707, 172-180.

Lu, X., Zhao, J., Wang, Z., Gan, B., Zhao, J., Kang, G., Zhang, X., 2020. Crystal plasticity finite element analysis of gradient nanostructured TWIP steel. International Journal of Plasticity 130.

Ma, A., Roters, F., Raabe, D., 2006. A dislocation density based constitutive model for crystal plasticity FEM including geometrically necessary dislocations. Acta Materialia 54, 2169-2179.

Marano, A., Gélébart, L., Forest, S., 2021. FFT-based simulations of slip and kink bands formation in 3D polycrystals: Influence of strain gradient crystal plasticity. Journal of the Mechanics and Physics of Solids 149.

Meng, B., Fu, M.W., Shi, S.Q., 2016. Deformation behavior and microstructure evolution in thermal-aided mesoforming of titanium dental abutment. Materials & Design 89, 1283-1293.

Meng, B., Wang, W.H., Zhang, Y.Y., Wan, M., 2019. Size effect on plastic anisotropy in microscale deformation of metal foil. Journal of Materials Processing Technology 271, 46-61.

Monk, J., Farkas, D., 2007. Tension–compression asymmetry and size effects in nanocrystalline Ni nanowires. Philosophical Magazine 87, 2233-2244.

NEMAT-NASSER, S., GUO, W.G., CHENG, J.Y., 1999. MECHANICAL PROPERTIES AND DEFORMATION MECHANISMS OF A COMMERCIALLY PURE TITANIUM. Acta Materialia 47, 3705-3720.

Nixon, M.E., Cazacu, O., Lebensohn, R.A., 2010. Anisotropic response of high-purity α-titanium: Experimental characterization and constitutive modeling. International Journal of Plasticity 26, 516-532.

Nye, J.F., 1953. Some geometrical relations in dislocated crystals. Acta Matallurgica 1, 153-162.

Paramatmuni, C., Zheng, Z., Rainforth, W.M., Dunne, F.P.E., 2020. Twin nucleation and variant selection in Mg alloys: An integrated crystal plasticity modelling and experimental approach. International Journal of Plasticity 135.

Peirce, D., Asaro, R.J., Needleman, A., 1982. An analysis of nonuniform and localized deformation in ductile single crystals. Acta Matallurgica 30, 1087-1119.

Qin, W., Li, J., Liu, Y., Kang, J., Zhu, L., Shu, D., Peng, P., She, D., Meng, D., Li, Y., 2019. Effects of grain size on tensile property and fracture morphology of 316L stainless steel. Materials Letters 254, 116-119.

Ravaji, B., Joshi, S.P., 2021. A crystal plasticity investigation of grain size-texture interaction in magnesium alloys. Acta Materialia 208.

Revil-Baudard, B., Cazacu, O., Flater, P., Chandola, N., Alves, J.L., 2016. Unusual plastic deformation and damage features in titanium: Experimental tests and constitutive modeling. Journal of the Mechanics and Physics of Solids 88, 100-122.

Sedaghat, O., Abdolvand, H., 2021. A non-local crystal plasticity constitutive model for hexagonal close-packed polycrystals. International Journal of Plasticity 136.

Sun, S.J., Tian, Y.Z., Lin, H.R., Yang, H.J., Dong, X.G., Wang, Y.H., Zhang, Z.F., 2018. Transition of twinning behavior in CoCrFeMnNi high entropy alloy with grain refinement. Materials Science and Engineering: A 712, 603-607.

Suryawanshi, J., Singh, G., Msolli, S., Jhon, M.H., Ramamurty, U., 2021. Tension-compression asymmetry and shear strength of titanium alloys. Acta Materialia 221.

Syed, F.W., Anil Kumar, V., Gupta, R.K., Kanjarla, A.K., 2019. Role of microstructure on the tension/compression asymmetry in a two-phase Ti-5Al-3Mo-1.5V titanium alloy. Journal of Alloys and Compounds 795, 151-162.

Tang, X.F., Peng, L.F., Shi, S.Q., Fu, M.W., 2019. Influence of crystal structure on size dependent deformation behavior and strain heterogeneity in micro-scale deformation. International Journal of Plasticity 118, 147-172.

Tang, X.F., Shi, S.Q., Fu, M.W., 2020. Interactive effect of grain size and crystal structure on deformation behavior in progressive micro-scaled deformation of metallic materials. International Journal of Machine Tools and Manufacture 148.

Tao, J., Gu, B., Chen, L., Zhou, J., 2019. Tension–Compression Asymmetry of Commercially Pure Titanium: Strain Rate Sensitivity and Microstructure Evolution. Jom 71, 2280-2290.

Taylor, G.I., 1934. The mechanism of plastic deformation of crystals. Part I.—Theoretical. Proceedings of the Royal Society of London. Series A, Containing Papers of a Mathematical and Physical Character 145.

Taylor, G.I., 1938. Plastic strain in metals. J. Inst. Metals 62, 307-324.

Tomé, C.N.T., Lebensohn, R.A., Kocks, U.F., 1991. A model for texture development dominated by deformation twinning application to zirconium alloys. Acta Metallurgica et Materialia 39, 2667-2680.

Vasilev, E., Knezevic, M., 2021. Role of microstructural heterogeneities in damage formation and fracture of oligocrystalline Mg under tensile loading. Materials Science and Engineering: A 827.

Venkatramani, G., Ghosh, S., Mills, M., 2007. A size-dependent crystal plasticity finite-element model for creep and load shedding in polycrystalline titanium alloys. Acta Materialia 55, 3971-3986.

Vollertsen, F., Schulze Niehoff, H., Hu, Z., 2006. State of the art in micro forming. International Journal of Machine Tools and Manufacture 46, 1172-1179.

Voyiadjis, G.Z., Song, Y., 2019. Strain gradient continuum plasticity theories: Theoretical, numerical and experimental investigations. International Journal of Plasticity 121, 21-75.

Warwick, J.L.W., Jones, N.G., Rahman, K.M., Dye, D., 2012. Lattice strain evolution during tensile and compressive loading of CP Ti. Acta Materialia 60, 6720-6731.

Wijnen, J., Peerlings, R.H.J., Hoefnagels, J.P.M., Geers, M.G.D., 2021. A discrete slip plane model for simulating heterogeneous plastic deformation in single crystals. International Journal of Solids and Structures 228.

Wong, S.L., Madivala, M., Prahl, U., Roters, F., Raabe, D., 2016. A crystal plasticity model for twinning- and transformation-induced plasticity. Acta Materialia 118, 140-151.

Wouters, O., Vellinga, W.P., Tijum, R.V., de Hosson, J.T.M., 2005. On the evolution of surface roughness during deformation of polycrystalline aluminum alloys. Acta Materialia 53, 4043-4050.

Wronski, M., Arul Kumar, M., Capolungo, L., McCabe, R.J., Wierzbanowski, K., Tomé, C.N., 2018. Deformation behavior of CP-titanium: Experiment and crystal plasticity modeling. Materials Science and Engineering: A 724, 289-297.

Wroński, M., Kumar, M.A., McCabe, R.J., Wierzbanowski, K., Tomé, C.N., 2022. Deformation behavior of CP-titanium under strain path changes: Experiment and crystal plasticity modeling. International Journal of Plasticity 148.

Wu, Z., Curtin, W.A., 2015. The origins of high hardening and low ductility in magnesium. Nature 526, 62-67.

Xu, J., Wang, X., Wang, C., Yuan, L., Chen, W., Bao, J., Su, Q., Xu, Z., Wang, C., Wang, Z., Shan, D., Guo, B., 2021a. A Review on Micro/Nanoforming to Fabricate 3D Metallic Structures. Adv Mater 33, e2000893.

Xu, Z., Li, Z., Zhang, R., Jiang, T., Peng, L., 2021b. Fabrication of micro channels for titanium PEMFC bipolar plates by multistage forming process. International Journal of Hydrogen Energy 46, 11092-11103.

Xu, Z.T., Peng, L.F., Fu, M.W., Lai, X.M., 2015. Size effect affected formability of sheet metals in micro/meso scale plastic deformation: Experiment and modeling. International Journal of Plasticity 68, 34-54.

Yalçinkaya, T., Özdemir, İ., Simonovski, I., 2017. Micromechanical modeling of intrinsic and specimen size effects in microforming. International Journal of Material Forming 11, 729-741.

Yang, H., Li, H., Ma, J., Wei, D., Chen, J., Fu, M.W., 2020. Temperature dependent evolution of anisotropy and asymmetry of α-Ti in thermomechanical working: Characterization and modeling. International Journal of Plasticity 127.

Yin, D.D., Boehlert, C.J., Long, L.J., Huang, G.H., Zhou, H., Zheng, J., Wang, Q.D., 2021. Tension-compression asymmetry and the underlying slip/twinning activity in extruded Mg–Y sheets. International Journal of Plasticity 136.

Yoo, M.H., 1981. Slip, Twinning, and Fracture in Hexagonal Close-Packed Metals. Metallurgical and Materials Transactions A 12, 409-418.

Yoshida, K., 2014. Effects of grain-scale heterogeneity on surface roughness and sheet metal necking. International Journal of Mechanical Sciences 83, 48-56.

Yun, W., Peilong, D., Zhenying, X., Hua, Y., Jiangping, W., Jingjing, W., 2010. A constitutive model for thin sheet metal in micro-forming considering first order size effects. Materials & Design 31, 1010-1014.

Zaefferer, S., 2003. A study of active deformation systems in titanium alloys dependence. Materials Science and Engineering: A 344, 20-30.

Zecevic, M., Beyerlein, I.J., Knezevic, M., 2017. Coupling elasto-plastic self-consistent crystal plasticity and implicit finite elements: Applications to compression, cyclic tension-compression, and bending to large strains. International Journal of Plasticity 93, 187-211.

Zhang, B., Meng, A.C., Meng, W.J., 2021. Deviation of mechanical behavior in microforming from continuum scaling: A geometrically necessary dislocation storage perspective. International Journal of Machine Tools and Manufacture 169.

Zhang, H., Dong, X., 2015. Physically based crystal plasticity FEM including geometrically necessary dislocations: Numerical implementation and applications in micro-forming. Computational Materials Science 110, 308-320.

Zhang, H., Liu, J., Sui, D., Cui, Z., Fu, M.W., 2018. Study of microstructural grain and geometric size effects on plastic heterogeneities at grain-level by using crystal plasticity modeling with high-fidelity representative microstructures. International Journal of Plasticity 100, 69-89.

Zhao, Z., Ramesh, M., Raabe, D., Cuitiño, A.M., Radovitzky, R., 2008. Investigation of three-dimensional aspects of grain-scale plastic surface deformation of an aluminum oligocrystal. International Journal of Plasticity 24, 2278-2297.

Zhu, C., Chen, Y., Xu, J., Yu, H., Shan, D., Guo, B., 2022. Grain size and specimen thickness effects on twinning behaviors in high strain rate deformation of ultra-thin pure titanium sheet. Materials Science and Engineering: A 832.